Computer Methods in Applied Mechanics and Engineering 437 (2025) 117756

Contents lists available at ScienceDirect

Comput. Methods Appl. Mech. Engrg.

journal homepage: www.elsevier.com/locate/cma

A coupled FEM-VEM approach for crack tracking in quasi-brittle materials

Antonino Spada [a,*], Marianna Puccia [a], Elio Sacco [b], Giuseppe Giambanco [a]

[a] Department of Engineering, University of Palermo, Viale delle Scienze, Ed. 8, 90128, Palermo, Italy
[b] Department of Structures for Engineering and Architecture, University of Naples Federico II, Via Claudio 21, 80125 Naples, Italy

ARTICLE INFO

Keywords:
Localization
Crack propagation
VEM
Interphase
Quasi-brittle materials
Isotropic damage model

ABSTRACT

The numerical simulation of crack propagation in quasi-brittle materials has historically been mainly faced by means of consolidated approaches in the framework of the finite element method (FEM). However, the very recently developed virtual element method (VEM) is a new promising technique whose strong point is the possibility to model polygonal meshes, characterized by any number of edges. This paper proposes a new approach, coupling FEM and VEM for crack tracking in quasi-brittle materials. In these materials, diffuse degradation is followed by high deformation bands localizing in certain regions of the structure. To best exploit the potentialities of FEM and VEM, in this work the structure is initially entirely modeled through a FEM mesh. Then, when a diffuse damage meets the requirements for a localized band formation, the involved finite elements are converted into virtual sub-elements among which a thin layer is introduced. The thin layer is modeled through interphase (IPH) elements, which are advanced mechanical devices with respect to the common interface elements since internal strains and stresses are added to the contact ones. The portion of the structure modeled using VEs and IPHs is called substructure. Structure and substructure are solved through two nested iterative procedures.

The proposed numerical and crack tracking strategy are illustrated in detail and the results on three benchmark examples show its applicability as an alternative strategy to the full FEM approach.

1. Introduction

Strain localization and fracture initiation are key failure modes in structures composed of quasi-brittle materials. The onset of localized deformations is seen as a result of the constitutive instability of the material, corresponding to a bifurcation point in the Lyapunov sense [1]. Several theoretical studies have been conducted to identify this bifurcation point and to describe the post-instability behavior of the material from both static and dynamic perspectives [2–8].

Various computational strategies have been proposed to address localization challenges in engineering problems. Generally, the evolution of localization can be described using three different approaches.

Continuum models treat the domain as a single, continuous entity, typically represented through advanced constitutive relations. These models may also incorporate nonlocal [9] or gradient-based [10] approaches, where the behavior of a material point is influenced by the response of neighboring points.

* Corresponding author.
E-mail addresses: antonino.spada@unipa.it (A. Spada), marianna.puccia@unipa.it (M. Puccia), elio.sacco@unina.it (E. Sacco), giuseppe.giambanco@unipa.it (G. Giambanco).

https://doi.org/10.1016/j.cma.2025.117756
Received 14 October 2024; Received in revised form 19 December 2024; Accepted 13 January 2025
Available online 30 January 2025

The Smeared Crack Model (SCM) [11] represents inelastic strains as distributed (smeared) throughout the structure. When the material no longer behaves as a continuum, discrete models are used, where the material is treated as a collection of separate blocks, as in the Discrete Element Method (DEM) [12]. In the context of meshless methods, the Cracking Particles Method (CPM) [13] and the Cracking Element Method (CEM) [14] have been proposed. These methods are based on a discontinuous crack model, where each element can crack independently of the others.

Finally, hybrid continuous/discontinuous models have been developed. Starting from a continuum, they introduce discontinuities through mechanical devices simulating strain localization. Hybrid models lump all nonlinearities into a discrete line or surface, which possesses its own constitutive law. We can generally refer this category to the so-called Cohesive Zone Models (CZM): a discontinuity is represented as a Zero-Thickness Interface (ZTI) where the displacement field is discontinuous, as firstly formulated by Barenblatt (1959) [15], Dugdale (1960) [16] or Hillerborg (1976) [17]. An interface model for both soft and hard damaging adhesives and including the effect of damage velocity has been recently proposed by Lebon et al. [18].

Within the framework of the Finite Element Method (FEM), two distinct approaches can be identified based on the location of the discontinuity: *interelement* and *intraelement* discontinuities. In the first approach, discontinuities are predefined between opposite sides of adjacent elements, which often requires a computationally expensive and fine mesh. In contrast, the second approach addresses this mesh-dependency by modifying the basic formulation to accommodate intraelement displacement or strain jumps, thus allowing for discontinuities within the elements themselves.

The eXtended-Finite Element Method (X-FEM) [19,20] or the Generalized Finite Element Method (G-FEM) [21,22] overcome the need for remeshing through a local enrichment procedure of the cracked elements related to the Partition of Unity Method (PUM), formulated by Babuška et al. in 1996 [23].

Recently, the Augmented-Finite Element Method (A-FEM) was proposed by Ling et al. [24–27]. This approach takes into account multiple intra-element discontinuities with arbitrary paths. This method uses standard finite element shape functions, so it essentially maintains the advantage of element locality and compatibility with existing standard FEM programs. Additional Dofs are inserted to describe the fracture but they are then condensed at the element equilibrium level. The cracked element is replaced with three new elements: the two sub-domains and the localization band, through which they interact.

Starting from the A-FEM formulation, the Advanced Augmented-Finite Element Method (AA-FEM) has been proposed in [28] with the aim to simulate a finite element with an embedded weak discontinuity which has been modeled as an InterPHase (IPH) element [29,30]. The IPH is implemented as a thin material layer, with a finite thickness. It represents an enhancement of the ZTI model, since it allows modeling not only the contact components but also the internal ones. This overcomes the need to introduce a specific cohesive law for the contact element, as well as reducing the number of parameters.

The Virtual Element Method (VEM), recently developed by Beirão Da Veiga et al. in 2013, is a generalization of the classic FEM [31–36]. Its principal feature is its great adaptability and flexibility, since it is capable of modeling polygonal meshes, characterized by any number of edges without constraints. This permits VEM to be more efficient with respect to classical FEM in mesh generation, also starting from irregular or distorted geometries.

With respect to the original version of the AA-FEM code in [28] and in order to overcome some of its deficiencies, it is now proposed a coupled FEM-VEM approach as the main novelty of this work. The term 'coupled' refers to the fact that, starting from an entire FE mesh at pristine conditions, those elements crossed by the crack are bit by bit transformed into virtual elements.

With respect to the original FEM-based code and exploiting the potentialities of the VEM, three main improvements are obtained:

- the crack tip can occupy a point inside the element and not only on the element edge as in the FEM-based code, where the fracturing element was entirely cut into three new elements at localization conditions;
- conformity of the mesh, since previously nodes on the crack tip were not constrained to remain on the edge of the adjacent element;
- the sub-elements can have any number of nodes and edges and can be treated as unique elements, while before non-standard sub-elements were generated by assembling triangular elements.

The proposed crack tracking algorithm is also new with respect to previous work, since it is based on a mix of local and nonlocal information rather than local only.

Finally, the virtual element is implemented according to the divergence-free polynomial representation of the enhanced VEM formulation proposed by [33,37]. With respect to the standard VEM, the enhanced VEM formulation gives the advantage of avoiding stiffness matrix stabilization and returns more accurate results.

The paper is organized as follows. Section 2 defines the problem to solve. In Section 3 the proposed crack-tracking strategy is presented, while Section 4 shows all the aspects of the numerical implementation of the approach, including the formulation of the VE and the IPH. In Section 5 details on the specific elasto-damaging constitutive model are provided and the results of three different applications to quasi-brittle materials are reported. Conclusions are given in Section 6, while Appendix gives some details on the evaluation of the VE integrals.

2. Problem definition

Let us consider a solid body Ω (Fig. 1). The solid is defined in the Euclidean space R^3, referred to the orthonormal frame $(0, \mathbf{e}_x, \mathbf{e}_y, \mathbf{e}_z)$, and is constituted by a strain softening material. Volume forces $\mathbf{f}$, tractions $\mathbf{t}$ on Γ_t and kinematic constraints $\mathbf{u} = \bar{\mathbf{u}}$ on Γ_u can lead to concentration of strains, damage nucleation and propagation of cracks. These inelastic phenomena do not usually extend to the entire structure, but involve restricted parts of the body. In this work a restricted zone of the body crossed by a single

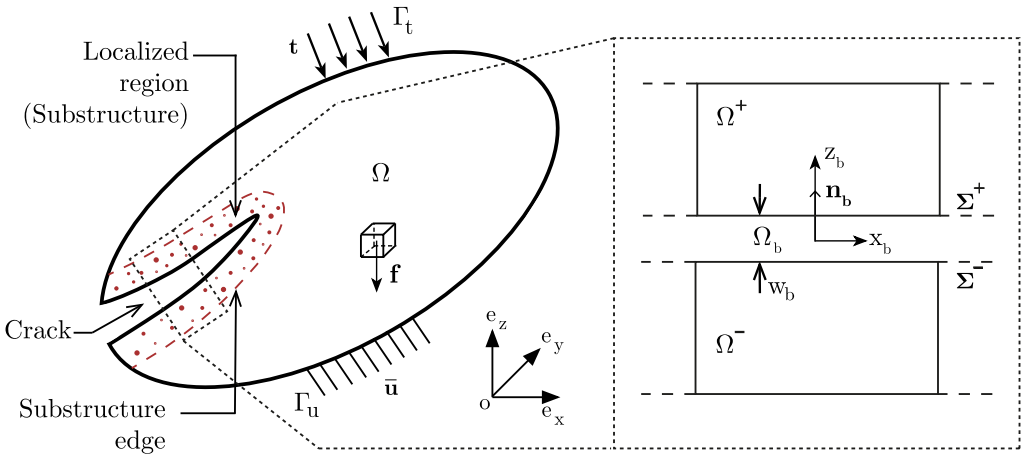

Fig. 1. Schematic representation of a structure with a localization band with zoom on a portion of the substructure.

crack is named 'substructure'.

Let us consider now a substructure crossed by a narrow zone Ω_b, simulating a crack, as in Fig. 1. The narrow zone separates the substructure into two parts Ω^+ and Ω^-. The thin material layer Ω_b has thickness w_b and is separated from the remaining parts Ω^+ and Ω^- by the weak discontinuity surfaces Σ^+, Σ^- where the displacement field is continuous and its gradient suffers discontinuity.

It is assumed that the band thickness is small if compared to the characteristic dimensions of the body, and is modeled using a local planar IPH element, neglecting any mechanical quantity related to band curvature. Ω^+ and Ω^- are numerically simulated employing virtual elements, while the rest of the body outside the substructure is modeled through more common finite elements. The use of virtual elements in the substructure is justified by the possible presence of elements with more than four nodes. For instance, the element containing the crack tip has seven nodes and seven edges, if the crack tip lies inside the element.

A local Cartesian coordinate system (x_b, y_b, z_b) is adopted to describe the mechanics at the localization band level, with x_b, y_b axes lying within the middle plane Σ_b of the joint and the z_b axis coinciding with the normal unit vector $\mathbf{n}_b$ directed towards the body Ω^+. The governing equations are:

$$
\begin{aligned}
&\boldsymbol{\varepsilon} = \mathbf{C}\,\mathbf{u} \\
&\mathbf{C}^T\,\boldsymbol{\sigma} + \mathbf{f} = \mathbf{0} \qquad \text{in } \Omega \\
&\boldsymbol{\sigma} = \mathbf{E}_s\,\boldsymbol{\varepsilon} \\
&\mathbf{C}_n^T\,\boldsymbol{\sigma} = \mathbf{t} \qquad \text{on } \Gamma_t \\
&\mathbf{u} = \bar{\mathbf{u}} \qquad \text{on } \Gamma_u
\end{aligned}
\tag{1}
$$

$$
\begin{aligned}
&\boldsymbol{\varepsilon}^{(-,+)} = \mathbf{C}\,\mathbf{u}^{(-,+)} \\
&\mathbf{C}^T\,\boldsymbol{\sigma}^{(-,+)} + \mathbf{f}^{(-,+)} = \mathbf{0} \qquad \text{in } \Omega^- \text{ and } \Omega^+ \\
&\boldsymbol{\sigma}^{(-,+)} = \mathbf{E}_s\,\boldsymbol{\varepsilon}^{(-,+)} \\
&\mathbf{C}_{n_b}^T\,\boldsymbol{\sigma}^{(-,+)} = \mathbf{q}^{(-,+)} \qquad \text{on } \Sigma^-,\ \Sigma^+
\end{aligned}
\tag{2}
$$

where $\boldsymbol{\sigma}$ and $\boldsymbol{\varepsilon}$ are the stress and strain fields respectively; $\mathbf{C}$, $\mathbf{C}_n$, and $\mathbf{C}_{n_b}$ compatibility matrices; $\mathbf{E}_s$ the secant elastic material tensor; $\mathbf{q}$ the traction at Σ^- and Σ^+ exchanged between Ω_b and Ω^- and Ω^+ respectively.

Fig. 2 illustrates the proposed strategy. At the beginning of the analysis no localization zone (and therefore no substructure) is present. The entire mesh is composed of FEs only (Fig. 2a). Load increasing causes damage onset in some of the FEs, until the first FE localizes. At this point, a substructure is created (colored elements in the Figure) containing that localized element only, which is converted into one VE with 7 nodes and an IPH (Fig. 2b). With the increase of the load, the crack advances in the element (Fig. 2c) and reaches the end of the element, while other elements localize and are added to the substructure (Fig. 2d–e). Completely fractured elements are treated as two VEs and an IPH. In this work, although the method has general validity and can be applied to quadrilateral FEs and triangular FEs as well, details for a quadrilateral FE mesh are given. As shown in Fig. 2, starting with quadrilateral FEs in non-localized conditions, the VEs can have 3, 4, 5, or 7 edges/nodes. The next subsection explains in detail the procedure applied to crack initiation and propagation, and in particular clarifies the criteria adopted for crack nucleation, orientation and extension.

The crack tracking procedure, the introduction of VEs, and the description of the localization band through an IPH element represent the key points of the proposed approach.

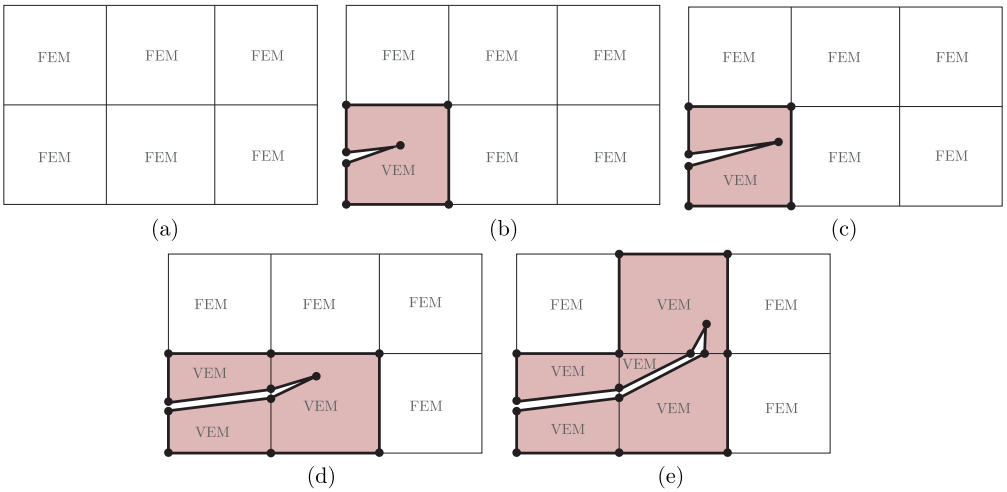

Fig. 2. Scheme of crack propagation with evidenced substructure configurations where FEs are converted into VEs and IPHs. (For interpretation of the references to color in this figure legend, the reader is referred to the web version of this article.)

3. Crack-tracking strategy

In continuous/discontinuous models, the proper simulation of crack nucleation and propagation is crucial for the goodness of the overall response.

A good crack tracking algorithm has to give answers to three questions: `when` to switch from a continuous to a discontinuous description of the element, `where` to locate the localization band, and `which` model has to be applied to better reproduce nonlinear phenomena. In the literature it is possible to qualitatively distinguish between three different categories of tracking algorithms: local/nonlocal, global or partial domain algorithms. The first ones compute locally the crack direction, using values referred to a single element or a restricted neighbor area [38]. The second ones compute simultaneously all the potential crack paths at each step of the analysis, by constructing a scalar function whose isolines represent the crack propagation directions within the whole structure [39]. Finally, the last ones solve a boundary value problem at each step within a sub-domain rather than in the whole structure [40].

The proposed procedure is built within a local/nonlocal approach for 2D structures where cracks nucleate and propagate on the basis of an elasto-damaging constitutive model representing material behavior.

In the following, details about the adopted criteria for crack nucleation and propagation are separately illustrated. The pseudo-code regarding the crack-tracking algorithm is shown in Algorithm 1.

3.1. Crack nucleation

Let us evaluate the volume average $\hat{D}$ of the damage variable in the nonlocalized finite element:

$$\hat{D} = \frac{1}{V_e} \int_{V_e} D \, \mathrm{d}\Omega, \tag{3}$$

where V_e is the volume of the finite element and D the damage developed in a point of the element.

Also, let $\boldsymbol{L}_b$ be the fracture tensor built on the principal strain directions $\mathbf{n}_i$ recorded at each element Gauss point, evaluated as:

$$\mathbf{L}_b = \frac{\sum_{i=1}^{ngp} D_i \, \mathbf{n}_i \, \mathbf{n}_i^T}{\sum_{i=1}^{ngp} D_i}, \tag{4}$$

with D_i the damage value at the same point and ngp the number of quadrature points.

The continuous–discontinuous transition takes place when $\hat{D}$ attains a critical value D_{crit}

$$\hat{D} = D_{crit}, \tag{5}$$

and contemporary when the localization direction $\mathbf{n}_b$, evaluated as the eigenvector associated with the maximum eigenvalue of the fracture tensor, does not differ significantly between two subsequent iterations (in other words when $\mathbf{n}_b$ is stabilized). Thus, in this work, critical damage is deemed as the parameter that attests to the passage to weak discontinuity as a result of localized strain.

When localization conditions are verified, a subsequent check is performed to fix the position of the crack tip. This check is based on the average damage $\hat{D}$ of the next potentially localized element. In this work the next potentially localized element is that element sharing one edge with the element containing the crack tip and where that edge holds the linear extension of the crack.

Algorithm 1 Crack-tracking algorithm

if no SUBS **then** ▷ Crack nucleation
  Evaluate $\hat{D}$ and $\mathbf{n}_b$
  if $\hat{D} = D_{crit}$ **then**
    Evaluate $\mathbf{x}_{bp}$ and identify the next potentially localized element
    if $\hat{D}_{next} \geq D_{min}$ **then** ▷ perform checks
      Cut entire element and locate crack tip on the next element
    else
      Locate crack tip within the element (partially cracked element)
    end if
  end if
else ▷ Crack propagation
  Evaluate $\hat{D}_{IPH-tip}$
  if $\hat{D}_{IPH-tip} < D_{stab}$ **then**
    Calculate $\boldsymbol{L}_b^{nl} \rightarrow \mathbf{n}_b$
  end if
  For fixed α calculate $r = \frac{\hat{D}_{IPH-tip}}{D_{crit}}\, d \leq d$
  if $(\hat{D} = D_{crit}).or.(d \leq L_{min})$ **then**
    identify the next potentially localized element
    if $\hat{D}_{next} \geq D_{min}$ **then** ▷ perform checks
      Cut entire element and locate crack tip on the next element
    else
      Locate crack tip within the element (partially cracked element)
    end if
  end if
end if

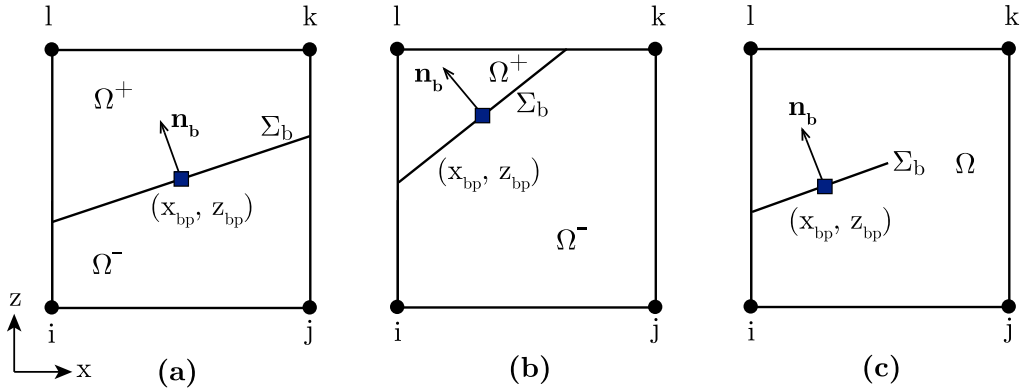

Fig. 3. Crack nucleation. FE crossed by the localization band and switched into (a–b) two VEs or (c) one VE and an interphase element after crack insertion.

As in the delayed crack models, if the average damage of the next potentially localized element reaches a threshold value D_{min}, the actual localized element undergoes a complete continuous-discontinuous transition. On the contrary, the crack tip is constrained to remain within the element, giving a not complete continuous-discontinuous transition (Fig. 3c). Since it is also assumed that the crack tip can be located in the finite element in a fixed number of positions in order to reduce the computational effort, in the case of a not complete continuous-discontinuous transition the crack tip is left to occupy the last available position in the element. If the transition is instead complete, the element can be divided into two quadrilateral VEs (Fig. 3a), or in a triangular and a pentagonal VEs (Fig. 3b).

For the first element of the substructure, in each one of the three cases showed in Fig. 3, a balance point having coordinates (x_{bp}, z_{bp}) needs to be initialized. This point is located through a damage-weighted average of the coordinates of the ngp integration points (x_i, z_i):

$$x_{bp} = \frac{\sum_{i=1}^{ngp} D_i\, x_i}{\sum_{i=1}^{ngp} D_i} \qquad z_{bp} = \frac{\sum_{i=1}^{ngp} D_i\, z_i}{\sum_{i=1}^{ngp} D_i}. \tag{6}$$

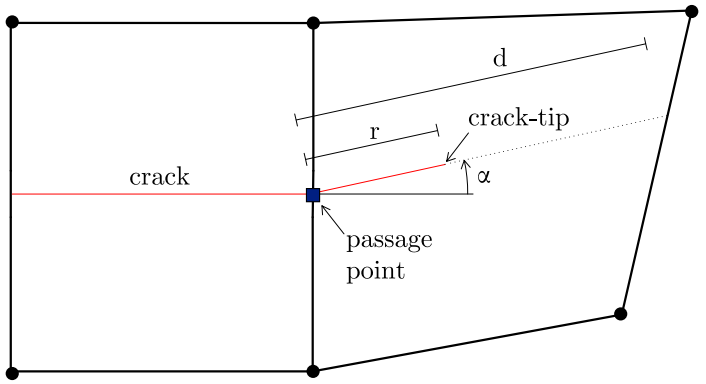

Fig. 4. Crack propagation scheme.

3.2. Crack propagation

After a crack is nucleated, its propagation is numerically governed by controlling two parameters only, namely crack inclination and extension. The crack tip is allowed to occupy a position inside the element and not always a point on its edge, as in the previous AA-FEM procedure [28].

With reference to Fig. 4, the passage point is fixed and coincident with the extreme point of the crack in the preceding localized element. Crack inclination is evaluated as the anti-clockwise angle α from the horizontal line. Crack extension r is the distance between the crack tip and the passage point for fixed α.

Crack orientation is evaluated in a nonlocal manner, as proposed in [40]. In particular, the nonlocal direction $\mathbf{n}_b$ is calculated through the spectral analysis of a nonlocal fracture tensor $\boldsymbol{L}_b^{nl}$ built over a semicircular domain A^{nl} of radius R centered on the passage point (Fig. 5). R is usually proportional to the element size. To avoid coming back fractures the half circle is orthogonal to the crack direction in the previous full localized element, and looks towards the crack front. $\boldsymbol{L}_b^{nl}$ is obtained as:

$$\mathbf{L}_b^{nl} = \frac{\int_{A^{nl}} \Psi\, \mathbf{n}\,\mathbf{n}^T \,\mathrm{d}A^{nl}}{\int_{A^{nl}} \Psi \,\mathrm{d}A^{nl}}, \tag{7}$$

with $\mathbf{n}$ the principal strain direction at the Gauss point and Ψ the associated weight, evaluated using the classical bell-shaped function:

$$\Psi = \begin{cases} \left[1 - \left(\frac{|\mathbf{x}-\mathbf{x}_{pp}|}{R}\right)^2\right]^2 & \text{if} \quad |\mathbf{x}-\mathbf{x}_{pp}| \le R \\ 0 & \text{if} \quad |\mathbf{x}-\mathbf{x}_{pp}| > R \end{cases} \tag{8}$$

with $\mathbf{x}$ the coordinates of a point inside the domain and $\mathbf{x}_{pp}$ the coordinates of the passage point.

During assembly of $\boldsymbol{L}_b^{nl}$, the contribution of the virtual element containing the crack tip is also included, by assuming a unitary weight and a unique fracture tensor for the entire element. The latter is evaluated by performing an integration over the element area of the punctual fracture tensor.

The crack can rotate inside the element between two subsequent time steps, remaining rectilinear. This is because crack orientation could not be optimal at the beginning of element cracking. As a consequence, the crack can rotate only within the element containing the crack tip, not in the remaining full cracked elements. A criterion is adopted whereby the crack is not stable until a damage threshold D_{stab} is reached. This threshold ensures that the crack has reached its optimal direction.

This approach adheres to the basic principles of the so-called Rotating Crack Models (RCM) [41], which are designed to overcome stress-locking issues arising when crack orientation is not allowed to rotate within an element.

Stress-locking can lead to non-physical stress concentrations around the crack, potentially hindering its propagation. By allowing for dynamic adjustment of crack direction and its progressive stabilization, RCM achieves a more realistic simulation of fracture mechanics without introducing propagation-blocking artifacts. This improves both the numerical performance and the physical accuracy of the crack evolution process.

The penetration length of the crack within the element is proportional to the average damage $\hat{D}_{IPH}$ of the IPH, since damage is frozen in the virtual element. $\hat{D}_{IPH}$ is evaluated as the mean value of the damages at the Gauss points of the IPH element containing the crack tip.

Therefore, the penetration distance r is evaluated as follows:

$$r = \frac{\hat{D}_{IPH}}{D_{crit}} d \le d, \tag{9}$$

being d the hypothetical maximum projected length of the crack within the element.

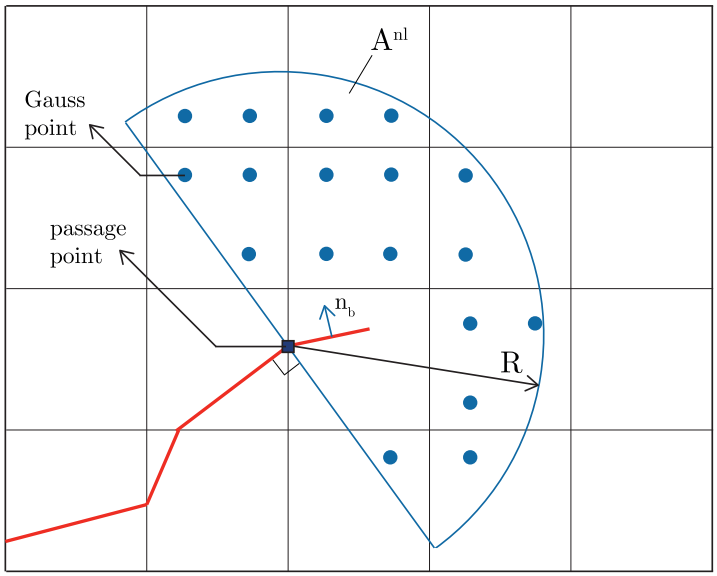

Fig. 5. Nonlocal domain for the evaluation of crack orientation.

When $r = d$, the check on $\hat{D}$ of the next potentially localized element is performed to establish if the element can be immediately cut or it is necessary to wait for some subsequent steps.

In some cases it can happen that d is very small, when the crack is too close to a node. This could imply crack locking, while damage continues to propagate at the evaluation points of the next element. To fix this problem, a check is performed on d. In particular, when d is less than a minimum length value L_{min}, chosen equal to the distance between a Gauss point and the closest node, and contemporary the average damage $\hat{D}$ of the next potentially localized element is greater than D_{min}, the element is immediately cut, independently of $\hat{D}_{IPH}$.

For all the VEs of the substructure, damage is frozen to the value at the time of fragmentation. On the contrary, damage can increase in IPHs.

4. Numerical implementation

In this approach, the solution of a numerical problem always starts in the framework of classical nonlinear FEM. Nonlinearity is included on the basis of the specific constitutive relations that best describe the analyzed materials.

Discretization of structural geometry initially follows common FE rules. This work has been developed considering an initial FE mesh consisting of linear quadrilateral elements only, but the versatility of the VEM does not exclude the possibility to discretize the domain with FEs of different geometry.

When the localization conditions described in the previous Section 3 are respected, localized elements are converted into VEs and IPHs and included into what is called 'substructure', that is a portion of the original mesh constituted by VEs and IPHs only. Outside the substructure the mesh remains made of nonlinear FEs.

Numerically, the problem consists of two nested Newton–Raphson procedures. The substructure is solved separately from the rest of the structure, and its results are then employed for the solution of the entire structure nonlinear problem.

In the substructure, when the original FE is fully cracked, virtual sub-elements can have a triangular, quadrilateral or pentagonal shape. The element containing the crack tip is studied, instead, as a unique VE having seven edges/nodes. A possible node numbering in the cases of an element split into two quadrilaterals and for the element with seven edges is shown in Fig. 6a–b.

In the following subsections, the formulations of a VE and the basic principles of an IPH are firstly presented. Then, the attention is focused on the solutions at the substructure and structure levels.

4.1. VE formulation

The proposal of this paper is to replace a localized FE with two sub-domains, modeled following the VE formulation, and an interposed IPH. Therefore, let us consider an element crossed by an IPH Ω_b that cuts the element into two sub-domains, Ω^+ and Ω^- respectively, as represented in Fig. 7.

For each sub-domain, the mechanical problem regards an element subjected to volume forces $\mathbf{f}$, tractions $\mathbf{t}$ on the lateral surfaces Γ_t and contact tractions $\mathbf{q}^{(-,+)}$ on the physical surfaces separating the sub-domain from the IPH element. Since the VEM flexibility, the elements of the mesh could possess a generic number of nodes.

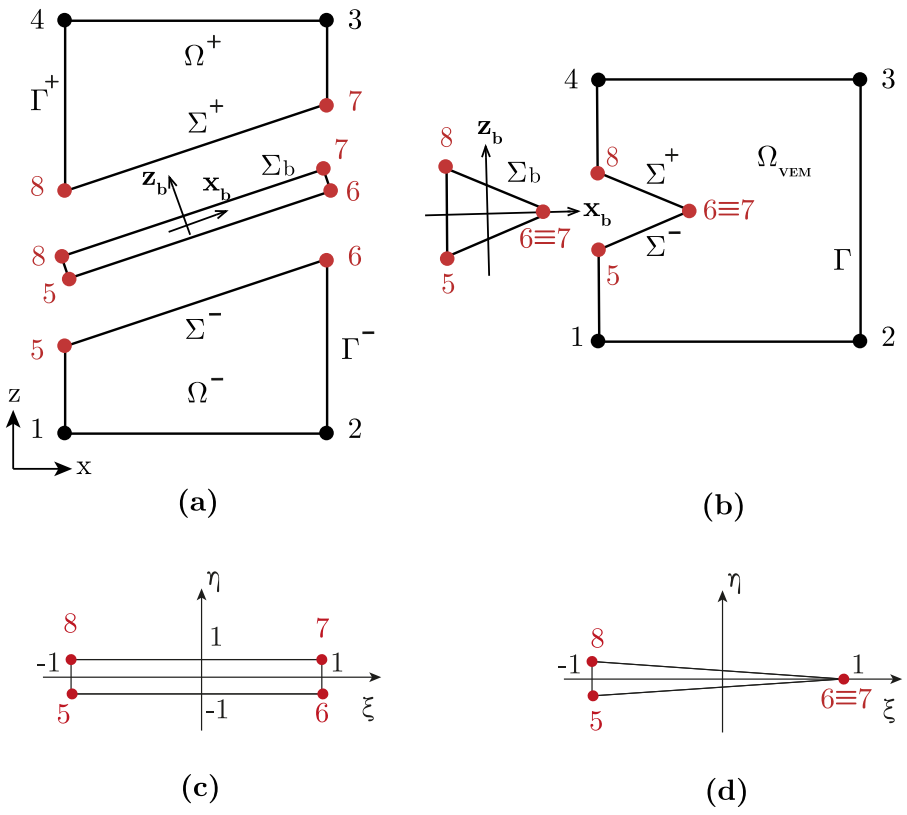

Fig. 6. Numbering of nodes in VE sub-domains and IPH: (a) full cracked element; (b) partially cracked element; (c) isoparametric representation of IPH of case (a); (d) isoparametric representation of IPH of case (b).

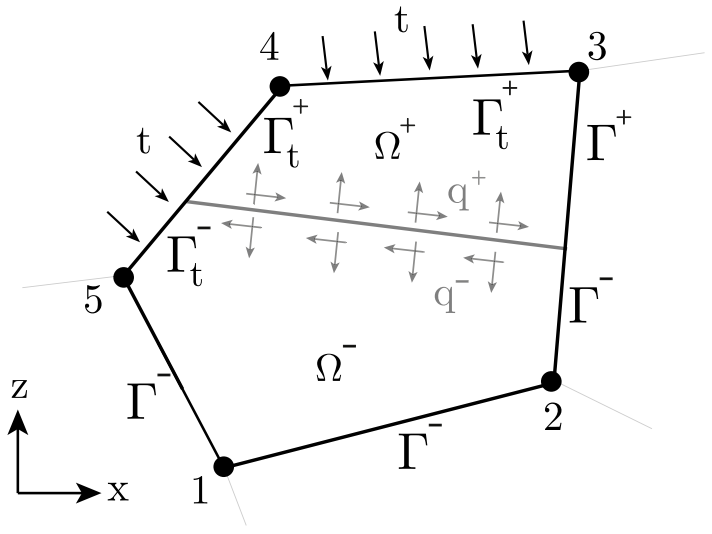

Fig. 7. Mechanical representation of the fragmentation of a FE in two VEs and an IPH.

Let us consider now a generic virtual element having area Ω_E, whose h stands for the associated mesh size and m corresponds to the number of edges. The displacement field $\mathbf{u}^h$ is not explicit in the interior of Ω_E. An explicit form for the displacement field $\tilde{\mathbf{u}}^h$ on the boundary Γ can be approximated as follows

$$\tilde{\mathbf{u}}^h = \tilde{\boldsymbol{N}}_b \, \mathbf{U}, \tag{10}$$

being $\tilde{\boldsymbol{N}}_b$ the matrix of polynomial functions on Γ and $\mathbf{U}$ the nodal displacements vector. Boundary shape functions in $\tilde{\boldsymbol{N}}_b$ are dependant on the degree k of the approximation. In the following, we will refer to the case $k = 1$, corresponding to piece-wise linear functions.

As the displacement field in the element is not explicitly assigned, the strain cannot be directly computed, but it has to be evaluated by a projection procedure. In fact, the strain is written in terms of the stress field $\boldsymbol{\sigma}$ by the constitutive equation:

$$\boldsymbol{\epsilon} = \mathbf{E}^{-1}\boldsymbol{\sigma} \tag{11}$$

with $\boldsymbol{\sigma}$ represented in the form:

$$\boldsymbol{\sigma} = \check{\mathbf{N}}\hat{\boldsymbol{\sigma}} \tag{12}$$

with $\check{\mathbf{N}}$ the matrix of the polynomial approximation of the stress and $\hat{\boldsymbol{\sigma}}$ the vector of the stress parameters. $\mathbf{E}$ is the elastic material tensor.

Then, the energy projection is performed by enforcing:

$$\int_{\Omega_E} \check{\mathbf{N}}^T \left(\mathbf{E}^{-1}\check{\mathbf{N}}\hat{\boldsymbol{\sigma}} - \mathbf{C}\mathbf{u}^h\right) \mathrm{d}\Omega = \mathbf{0} \tag{13}$$

where $\mathbf{C}$ is the compatibility differential operator, i.e.:

$$\mathbf{C} = \begin{bmatrix} \frac{\partial}{\partial x} & 0 \\ 0 & \frac{\partial}{\partial z} \\ \frac{\partial}{\partial z} & \frac{\partial}{\partial x} \end{bmatrix}. \tag{14}$$

By invoking the divergence theorem, Eq. (13) leads to:

$$\int_{\Omega_E} \check{\mathbf{N}}^T\mathbf{E}^{-1}\check{\mathbf{N}}\,\hat{\boldsymbol{\sigma}}\mathrm{d}\Omega = \int_{\Gamma} \check{\mathbf{N}}^T\mathbf{N}_E\tilde{\mathbf{u}}^h\mathrm{d}\Gamma - \int_{\Omega_E} \left(\mathbf{C}^T\check{\mathbf{N}}\right)^T\mathbf{u}^h\mathrm{d}\Omega \tag{15}$$

where $\mathbf{C}^T$ represents (in the Voigt notation) the divergence operator and $\mathbf{N}_E$ is the matrix associated to the outward normal unit vector, i.e.:

$$\mathbf{N}_E = \begin{bmatrix} n_x & 0 \\ 0 & n_z \\ n_z & n_x \end{bmatrix}. \tag{16}$$

The last term of Eq. (15) can be conveniently eliminated by selecting the terms of the polynomial stress approximation so that $\mathbf{C}^T\check{\mathbf{N}} = \mathbf{0}$, i.e. the stress is divergence-free. Recalling the representation of the displacement on the element boundary (10), Eq. (15) gives:

$$\hat{\boldsymbol{\sigma}} = \mathbf{G}^{-1}\,\mathbf{B}\,\mathbf{U} \qquad \text{with } \mathbf{G} = \int_{\Omega_E} \check{\mathbf{N}}^T\mathbf{E}^{-1}\check{\mathbf{N}}\mathrm{d}\Omega, \quad \mathbf{B} = \int_{\Gamma} \check{\mathbf{N}}^T\mathbf{N}_E\tilde{\boldsymbol{N}}_b\mathrm{d}\Gamma. \tag{17}$$

Finally, substituting the expression (17) into the formula (12), the strain (11) takes the form:

$$\boldsymbol{\epsilon} = \mathbf{E}^{-1}\,\check{\mathbf{N}}\,\mathbf{G}^{-1}\,\mathbf{B}\,\mathbf{U} \tag{18}$$

representing the strain written as a function of the displacements at the boundary nodes of the element only.

Once the value of k is set (as declared above $k = 1$), a very important point is the right choice of the approximation matrix $\check{\mathbf{N}}$. In fact, depending on the number of the boundary nodes of the element, the right choice of $\check{\mathbf{N}}$ can ensure the stability of the element without introducing further terms [33–35].

Now, let us write the Principle of Virtual Displacements (PVD) to the VE. It reads:

$$\int_{\Omega_E} \left(\delta\mathbf{u}^h\right)^T\mathbf{f}\,\mathrm{d}\Omega + \int_{\Gamma_t} \left(\delta\tilde{\mathbf{u}}^h\right)^T\mathbf{t}\,\mathrm{d}\Gamma + \int_{\Sigma_b} \left(\delta\tilde{\mathbf{u}}^h\right)^T\mathbf{q}\,\mathrm{d}\Sigma = \int_{\Omega_E} \delta\boldsymbol{\epsilon}^T\boldsymbol{\sigma}\,\mathrm{d}\Omega. \tag{19}$$

By substituting relation (17) in (12) and considering expression (18), the internal work at the right hand side of equality (19) can be rewritten, conducting to the following expression of the element consistent stiffness matrix:

$$\mathbf{K}_{VE} = \boldsymbol{B}^T\boldsymbol{G}^{-T}\left(\int_{\Omega_E} \check{\boldsymbol{N}}^T\boldsymbol{E}^{-1}\check{\boldsymbol{N}}\,\mathrm{d}\Omega\right)\boldsymbol{G}^{-1}\boldsymbol{B}. \tag{20}$$

If body forces are neglected, as in this work, the virtual element force vector is given by:

$$\mathbf{F}_{VE} = \int_{\Gamma_t} \left(\tilde{\boldsymbol{N}}_b\right)^T\mathbf{t}\,\mathrm{d}\Gamma + \int_{\Sigma_b} \left(\tilde{\boldsymbol{N}}_b\right)^T\mathbf{q}\,\mathrm{d}\Sigma. \tag{21}$$

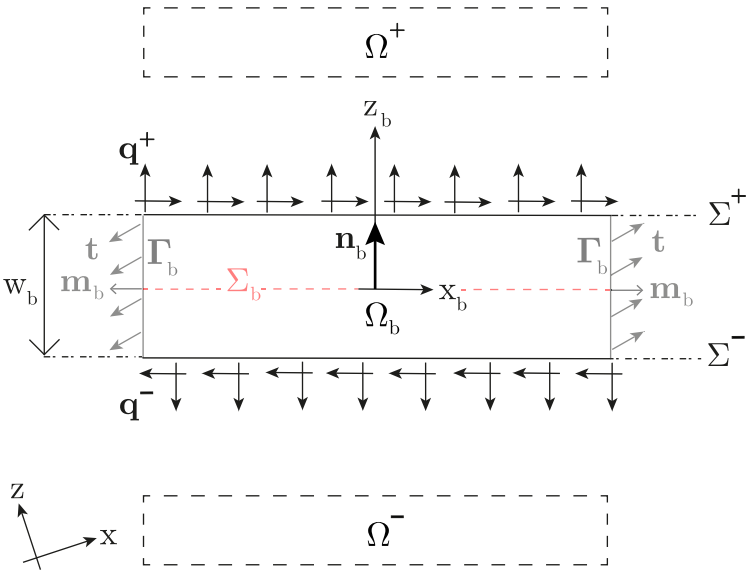

Fig. 8. Mechanical representation of the interphase.

4.2. Interphase element formulation

An IPH element is a numerical device that simulates weak and thin material layers or localization bands on a continuum.

In this subsection the IPH main assumptions and governing equations are recalled. Details can be found in [28,30].

With reference to Fig. 8, an IPH is a thin material layer Ω_b of finite thickness w_b, which is small if compared to the characteristic dimensions of the body. Ω_b is separated from the sub-domains Ω^+ and Ω^- by two weak discontinuity surfaces Σ^+ and Σ^-, where the displacement field is continuous while the strain has a jump.

For 2D problems, static and kinematic equations are written with reference to a local Cartesian coordinate system (x_b, z_b), where x_b axis lies within the middle plane Σ_b of the band and the z_b axis is along the normal unit vector $\mathbf{n}_b$ directed towards the sub-domain Ω^+. The thin layer is subjected to external tractions $\mathbf{t}$ on the lateral surface Γ_b (identified by the normal unit vector $\mathbf{m}_b$) and to the contact tractions $\mathbf{q}^+$ and $\mathbf{q}^-$ on the physical surfaces Σ^+ and Σ^-, respectively. Body forces are neglected.

In agreement with the formulation in [29,42], let us consider the following assumptions:

- the band thickness is small if compared to the characteristic dimensions of the remaining part of the body, so that it is numerically possible to flatten the interphase element on its middle surface Σ_b;
- the interphase element is planar, so any mechanical quantities referred to the band curvature are neglected;
- the fibers along z_b are maintained rectilinear during the deformation process, so the displacement field $\mathbf{u}_b$ is a linear function of the displacements $\mathbf{u}_b^+$ and $\mathbf{u}_b^-$ in Σ^+ and Σ^-:

$$\mathbf{u}_b\left(x_b, z_b\right) = \left(\frac{1}{2} + \frac{z_b}{w_b}\right)\mathbf{u}_b^+\left(x_b\right) + \left(\frac{1}{2} - \frac{z_b}{w_b}\right)\mathbf{u}_b^-\left(x_b\right); \tag{22}$$

- the strain state is uniform in the band thickness and can be considered equal to the average value along the z_b direction:

$$\boldsymbol{\varepsilon}_b(x_b) = \frac{1}{w_b}\int_{\frac{-w_b}{2}}^{\frac{w_b}{2}} \boldsymbol{C}\mathbf{u}_b(x_b, z_b)\,\mathrm{d}z_b, \tag{23}$$

where $\boldsymbol{C}$ is the compatibility matrix defined in Eq. (14).

By imposing the PVD, the following equilibrium equations of the IPH are derived:

$$\mathbf{q}^+ - \mathbf{C}_{n_b}^T\boldsymbol{\sigma}_b + \frac{w_b}{2}\mathbf{C}^T\boldsymbol{\sigma}_b = \mathbf{0} \quad \text{on } \Sigma^+ \tag{24}$$

$$\mathbf{q}^- + \mathbf{C}_{n_b}^T\boldsymbol{\sigma}_b + \frac{w_b}{2}\mathbf{C}^T\boldsymbol{\sigma}_b = \mathbf{0} \quad \text{on } \Sigma^- \tag{25}$$

$$\mathbf{C}_{m_b}^T\boldsymbol{\sigma}_b = \mathbf{t} \quad \text{on } \Gamma_b \tag{26}$$

where $\mathbf{C}_{n_b}$ and $\mathbf{C}_{m_b}$ represent the compatibility matrices associated to the unit vectors $\mathbf{n}_b$ and $\mathbf{m}_b$ respectively, and $\boldsymbol{\sigma}_b$ is the stress vector.

The IPH has been numerically implemented following an isoparametric formulation. It is necessary to distinguish between the case of an IPH with four independent nodes (Fig. 6-c) and the case of an IPH where the nodes on the crack tip are constrained to

coincide until the crack tip reaches the element edge (Fig. 6-d). The difference between the two cases consists in the existence of a slave node (node 7 in the Figure) whose coordinates and displacements are the same as its master node (node 6 in the Figure).

For the case of an IPH with four nodes, the displacements on the physical surfaces $\Sigma^{(-,+)}$ can be collected in the two vectors $\overline{\mathbf{U}}_b^-$ and $\overline{\mathbf{U}}_b^+$ respectively, where the symbol $(\overline{*})$ means that the relative quantity is referred to the local interphase coordinate system. In this way, the strain field at the IPH can be written as

$$\boldsymbol{\epsilon}_b = \mathbf{B}_b^+ \overline{\mathbf{U}}_b^+ + \mathbf{B}_b^- \overline{\mathbf{U}}_b^- \tag{27}$$

with $\mathbf{B}_b^-$ and $\mathbf{B}_b^+$ compatibility matrices related to nodal displacements.

By following the same mathematical passages shown in [28], the following equilibrium equations for the IPH element hold:

$$\overline{\mathbf{K}}_b^{++} \overline{\mathbf{U}}_b^+ + \overline{\mathbf{K}}_b^{+-} \overline{\mathbf{U}}_b^- = \overline{\mathbf{F}}_b^+ \tag{28}$$

$$\overline{\mathbf{K}}_b^{-+} \overline{\mathbf{U}}_b^+ + \overline{\mathbf{K}}_b^{--} \overline{\mathbf{U}}_b^- = \overline{\mathbf{F}}_b^- \tag{29}$$

where

$$\overline{\mathbf{K}}_b^{++} = \int_{\Sigma_b} w_b \, \mathbf{B}_b^{+T} \mathbf{E}_t \, \mathbf{B}_b^+ \mathrm{d}\Sigma \qquad \overline{\mathbf{K}}_b^{+-} = \int_{\Sigma_b} w_b \, \mathbf{B}_b^{+T} \mathbf{E}_t \, \mathbf{B}_b^- \mathrm{d}\Sigma \tag{30}$$

$$\overline{\mathbf{K}}_b^{-+} = \int_{\Sigma_b} w_b \, \mathbf{B}_b^{-T} \mathbf{E}_t \, \mathbf{B}_b^+ \mathrm{d}\Sigma \qquad \overline{\mathbf{K}}_b^{--} = \int_{\Sigma_b} w_b \, \mathbf{B}_b^{-T} \mathbf{E}_t \, \mathbf{B}_b^- \mathrm{d}\Sigma \tag{31}$$

$$\overline{\mathbf{F}}_b^+ = \int_{\Sigma^+} \mathbf{N}_b^{+T} \mathbf{q}^+ \, \mathrm{d}\Sigma \qquad \overline{\mathbf{F}}_b^- = \int_{\Sigma^-} \mathbf{N}_b^{-T} \mathbf{q}^- \, \mathrm{d}\Sigma, \tag{32}$$

being $\boldsymbol{E}_t$ the tangent stiffness matrix, and $\mathbf{N}_b^{-,+}$ shape function matrices.

For the case shown in Fig. 6d, where node 7 coincides with node 6, it is more convenient to group the displacements of the IPH nodes in a unique vector $\overline{\mathbf{U}}_b$.

The equilibrium equations of the IPH are, in this case:

$$\overline{\mathbf{K}}_b \, \overline{\mathbf{U}}_b = \overline{\mathbf{F}}_b, \tag{33}$$

with

$$\overline{\mathbf{K}}_b = \int_{\Sigma_b} w_b \, \mathbf{B}^T \, \mathbf{E}_t \, \mathbf{B} \, d\Sigma \tag{34}$$

and

$$\overline{\mathbf{F}}_b = \int_{\Sigma^-} \left(\mathbf{N}_b^- \mathbf{S}^- \right)^T \mathbf{q}^- \, d\Sigma + \int_{\Sigma^+} \left(\mathbf{N}_b^+ \mathbf{S}^+ \right)^T \mathbf{q}^+ \, d\Sigma. \tag{35}$$

$\mathbf{B}$ is the IPH compatibility matrix, while $\mathbf{S}^-$ and $\mathbf{S}^+$ two selectivity matrices:

$$\mathbf{S}^- = \begin{bmatrix} \mathbf{I} & \mathbf{0} & \mathbf{0} \\ \mathbf{0} & \mathbf{I} & \mathbf{0} \end{bmatrix}, \quad \mathbf{S}^+ = \begin{bmatrix} \mathbf{0} & \mathbf{I} & \mathbf{0} \\ \mathbf{0} & \mathbf{0} & \mathbf{I} \end{bmatrix}. \tag{36}$$

4.3. Assembly routine and iterative solution at the substructure level

In the classical A-FEM approach, sub-elements and contact device are re-assembled in order to obtain the overall stiffness matrix of the localized element. A subsequent static condensation of the stiffness matrix eliminates dependence on the added nodes. In the proposed approach, the assembly routine involves VEs and IPH, and needs to be differentiated between totally and partially cracked elements.

Assembly routine has been deeply illustrated in [28]. Here, the main equations are given for the sake of completeness and to make this work self-contained.

In the case of a totally cracked element (Fig. 6a), it is necessary to assemble the stiffness matrix and force vector of three elements, namely the two VEs Ω^+ and Ω^- and the IPH. If the nodes are separated into external ($\mathbf{U}_e$) and band ($\mathbf{U}_b$) nodes and the stiffness matrices and force vectors are accordingly partitioned, after some mathematical manipulation the following equilibrium equations of the assembled element are obtained:

$$\begin{bmatrix} \mathbf{K}^{ee} & \mathbf{K}^{eb} \\ \mathbf{K}^{be} & \mathbf{K}^{bb} \end{bmatrix} \begin{bmatrix} \mathbf{U}_e \\ \mathbf{U}_b \end{bmatrix} = \begin{bmatrix} \mathbf{F}_e \\ \mathbf{0} \end{bmatrix}, \tag{37}$$

where

$$\mathbf{K}^{ee} = \begin{bmatrix} \mathbf{K}_{\Omega^-}^{ee} & \mathbf{0} \\ \mathbf{0} & \mathbf{K}_{\Omega^+}^{ee} \end{bmatrix}, \tag{38}$$

$$\mathbf{K}^{eb} = \begin{bmatrix} \mathbf{K}_{\Omega^-}^{eb} \, \mathbf{A} & \mathbf{0} \\ \mathbf{0} & \mathbf{K}_{\Omega^+}^{eb} \, \mathbf{A} \end{bmatrix}, \tag{39}$$

$$\mathbf{K}^{be} = \begin{bmatrix} \mathbf{K}^{be}_{\Omega^-} & \mathbf{0} \\ \mathbf{0} & \mathbf{K}^{be}_{\Omega^+} \end{bmatrix}, \tag{40}$$

$$\mathbf{K}^{bb} = \begin{bmatrix} \mathbf{K}^{bb}_{\Omega^-}\,\mathbf{A} - \mathbf{A}\,\mathbf{K}^{--}_{b} & -\mathbf{A}\,\mathbf{K}^{-+}_{b} \\ -\mathbf{A}\,\mathbf{K}^{+-}_{b} & \mathbf{K}^{bb}_{\Omega^+}\,\mathbf{A} - \mathbf{A}\,\mathbf{K}^{++}_{b} \end{bmatrix}. \tag{41}$$

In the above equations $\mathbf{K}^{ee}_{\Omega^{(-,+)}}$, $\mathbf{K}^{eb}_{\Omega^{(-,+)}}$, $\mathbf{K}^{be}_{\Omega^{(-,+)}}$, and $\mathbf{K}^{bb}_{\Omega^{(-,+)}}$ are the partitions of the stiffness matrices in Ω^- and Ω^+ with respect to the external and band degrees of freedom. $\mathbf{K}^{--}_b$, $\mathbf{K}^{-+}_b$, $\mathbf{K}^{+-}_b$, and $\mathbf{K}^{++}_b$ are the partitions of the IPH stiffness matrix with respect to nodes in Σ^- and Σ^+. $\mathbf{F}_e$ is the external force vector of the assembled element and

$$\mathbf{A} = \begin{bmatrix} \mathbf{0} & \mathbf{I} \\ \mathbf{I} & \mathbf{0} \end{bmatrix} \tag{42}$$

an operator used to respect the anticlockwise order of nodes, with $\mathbf{0}$ and $\mathbf{I}$ being the 2×2 null and identity matrices, respectively.

In the case of a partially cracked element (Fig. 6b), it is necessary to assemble stiffness matrix and force vector of two elements, Ω_{VEM} and an IPH, obtaining:

$$\begin{bmatrix} \mathbf{K}^{ee}_{VE} & \mathbf{K}^{eb}_{VE}\,\hat{\mathbf{A}} \\ \mathbf{K}^{be}_{VE} & \mathbf{K}^{bb}_{VE}\,\hat{\mathbf{A}} - \hat{\mathbf{A}}\,\mathbf{K}_b \end{bmatrix} \begin{bmatrix} \mathbf{U}_e \\ \mathbf{U}_b \end{bmatrix} = \begin{bmatrix} \mathbf{F}_e \\ \mathbf{0} \end{bmatrix}, \tag{43}$$

where $\hat{\mathbf{A}}$ is defined as

$$\hat{\mathbf{A}} = \begin{bmatrix} \mathbf{0} & \mathbf{0} & \mathbf{I} \\ \mathbf{0} & \mathbf{I} & \mathbf{0} \\ \mathbf{I} & \mathbf{0} & \mathbf{0} \end{bmatrix}. \tag{44}$$

At the generic step of the nonlinear process, all the elements constituting the substructure are assembled to obtain the equilibrium equations of the substructure:

$$\mathbf{K}_{SUB}\,\mathbf{U}_{SUB} = \mathbf{F}_{SUB}, \tag{45}$$

where

$$\mathbf{U}_{SUB} = \begin{bmatrix} \mathbf{U}^{SUB}_e \\ \mathbf{U}^{SUB}_i \end{bmatrix} \quad \text{and} \quad \mathbf{F}_{SUB} = \begin{bmatrix} \mathbf{F}^{SUB}_e \\ \mathbf{0} \end{bmatrix}, \tag{46}$$

with the subscript e to refer to the external degrees of freedom of the substructure, coincident with the degrees of freedom of the FEs of the structure before localization, and the subscript i to refer to the internal degrees of freedom of the substructure, coincident with the degrees of freedom of the added nodes.

In Eq. (45), $\mathbf{U}^{SUB}_e$ are imposed from the solution at the structure level. $\mathbf{F}^{SUB}_e$ and $\mathbf{U}^{SUB}_i$ are instead unknowns. In particular, $\mathbf{F}^{SUB}_e$ are transferred to the global structure as internal forces and used for the convergence of the global iterative nonlinear problem.

The pseudo-code for the solution of the equilibrium problem at the substructure level is reported in Algorithm 2. When the code used to solve the nonlinear problem at the substructure level is called, the displacements of the external nodes of the substructure are read, together with damages at VEs and IPH evaluation points. With damages in hand, an initial secant stiffness matrix is built. Displacements are transferred to the substructure in the form of the sum of displacements at the end of the previous step and increments at the actual step. The displacements at the end of the previous step are imposed in the equilibrium equations to initialize all other substructure variables, in particular the displacements of the internal nodes and the force vector of the external nodes. When displacements of internal nodes are known, damage at IPHs is again calculated and the secant stiffness matrix is substituted for the tangent one. At this point an elastic prediction is performed, by imposing the increments of the displacements at the external nodes and calculating the increments of the displacements for the internal nodes and of the forces for the external nodes. The total displacements for internal nodes permit updating damages at the IPHs and again the tangent stiffness matrix. At the end of the elastic prediction phase an error vector given by the difference between the substructure's external and internal force vectors permits checking convergence. If not, the subsequent nonlinear correction phase repeats the sequence of commands in order to update the displacements for internal nodes, the forces for external nodes, damages at the IPH evaluation points, stiffness matrix and error vector until convergence is reached. At convergence, the stiffness matrix and the force vector of the external nodes are passed to the global structure to assemble the structural stiffness matrix and internal force vector in order to solve the structure nonlinear problem.

Details on the integration of the stiffness matrix for the VEs are given in Appendix.

4.4. Iterative solution at the structural level

The solution of the nonlinear problem at the structural level follows the common rules of a Newton–Raphson iterative method, and is schematized in Algorithm 3. Assuming you know all the variables from the previous step $n-1$, these are used to initialize the correspondent variables at the beginning of the actual step n. By imposing the increments of the displacements in the constrained parts of the structure in a displacement driven procedure and/or the increments of the external forces in the loaded parts of the

Algorithm 2 Solution at the substructure level - SOLVE-SUBS

Read displacements at external nodes ($\mathbf{U}_e^{SUB} = \mathbf{U}_e^{SUB,prec} + \Delta\mathbf{U}_e^{SUB}$)
Read damages at the previous step
▶ **INITIALIZATION**
Initialize the stiffness matrix $\mathbf{K}_{SUB}^{(0)}$ from VEs and IPHs
Solve $\mathbf{K}_{SUB}^{(0)} \begin{bmatrix} \mathbf{U}_e^{SUB,prec} \\ \mathbf{U}_i^{SUB,(0)} \end{bmatrix} = \begin{bmatrix} \mathbf{F}_e^{SUB,(0)} \\ \mathbf{0} \end{bmatrix} \rightarrow \mathbf{U}_i^{SUB,(0)}$ and $\mathbf{F}_e^{SUB,(0)}$
Update damages at IPHs and $\mathbf{K}_{SUB}^{(0)}$
▶ **ELASTIC PREDICTION**
Set $j \leftarrow 1$
Solve $\mathbf{K}_{SUB}^{(0)} \begin{bmatrix} \Delta\mathbf{U}_e^{SUB} \\ \Delta\mathbf{U}_i^{SUB,(j)} \end{bmatrix} = \begin{bmatrix} \Delta\mathbf{F}_e^{SUB,(j)} \\ \mathbf{0} \end{bmatrix} \rightarrow \Delta\mathbf{U}_i^{SUB,(j)}$ and $\Delta\mathbf{F}_e^{SUB,(j)}$
$\mathbf{U}_i^{SUB,(j)} \leftarrow \mathbf{U}_i^{SUB,(0)} + \Delta\mathbf{U}_i^{SUB,(j)}$
$\mathbf{F}_e^{SUB,(j)} \leftarrow \mathbf{F}_e^{SUB,(0)} + \Delta\mathbf{F}_e^{SUB,(j)}$
Update damages at IPHs and calculate $\mathbf{K}_{SUB}^{(j)}$ and internal forces $\mathbf{F}_{int}^{SUB,(j)}$
Evaluate error $\mathbf{Err}^{(j)} = \mathbf{F}_{SUB}^{(j)} - \mathbf{F}_{int}^{SUB,(j)}$
if $\left|\mathbf{Err}^{(j)}\right| \geq tol$ **then** ▷ check convergence
▶ **NONLINEAR CORRECTION**
  $j \leftarrow j + 1$
  Solve $\mathbf{K}_{SUB}^{(j-1)} \begin{bmatrix} \mathbf{0} \\ \Delta\Delta\mathbf{U}_i^{SUB,(j)} \end{bmatrix} = \mathbf{Err}^{(j)} + \begin{bmatrix} \Delta\Delta\mathbf{F}_e^{SUB,(j)} \\ \mathbf{0} \end{bmatrix} \rightarrow \Delta\Delta\mathbf{U}_i^{SUB,(j)}$ and $\Delta\Delta\mathbf{F}_e^{SUB,(j)}$
  $\mathbf{U}_i^{SUB,(j)} \leftarrow \mathbf{U}_i^{SUB,(j-1)} + \Delta\Delta\mathbf{U}_i^{SUB,(j)}$
  $\mathbf{F}_e^{SUB,(j)} \leftarrow \mathbf{F}_e^{SUB,(j-1)} + \Delta\Delta\mathbf{F}_e^{SUB,(j)}$
  Update damages at IPHs and calculate ($\mathbf{K}_{SUB}^{(j)}$, $\mathbf{F}_{int}^{SUB,(j)}$)
  Evaluate error $\mathbf{Err}^{(j-1)} = \mathbf{F}_{SUB}^{(j)} - \mathbf{F}_{int}^{SUB,(j)}$
  go to 12
end if
$\mathbf{K}_{SUB}^{(j)}$ and $\mathbf{F}_e^{SUB,(j)}$ are transferred to the global structure.

structure in a force driven procedure, the total displacements and forces are calculated at the end of the elastic prediction. On the basis of the adopted constitutive model, the updated values of nodal displacements permit to evaluate the inelastic parameters at the evaluation points of each element. In this work an elasto-damaging constitutive model is used, but it is important to remark that every kind of nonlinear model could be implemented to properly catch the behavior of the specific studied material.

If a substructure is already present, the subroutine shown in Algorithm 2 is called by giving in input the displacements of its external nodes. The output of the subroutine is given in terms of a stiffness matrix and internal force vector for the substructure. These are assembled into the stiffness matrix and internal force vector of the structure.

The difference between the external force vector and the internal force vector defines the error vector whose modulus needs to be less than a tolerance value to ensure convergence. In those cases when convergence is still not reached, a nonlinear correction phase takes place and the operations from the solution of the equilibrium system to the building of the error vector are repeated. The employment of the updated tangent stiffness matrix at each iteration ensures quadratic convergence of the iterative process.

At convergence, crack-tracking Algorithm 1 is called to establish if a crack nucleates or propagates. When the penetration distance of the crack inside an element increases and/or the localization angle changes, the actual step needs to be entirely repeated starting from the values at the previous step, since a different geometry characterizes the structure.

5. Numerical applications

The effectiveness of the proposed approach has been tested through three numerical applications in combined mode I-mode II loading stress states.

Each application has been run under plane stress conditions and under displacement control.

Since the simulated materials can be classified among quasi-brittle materials, the Isotropic Damage Model formulated by Jirásek [43] and Mazars [44] has been chosen as the constitutive model. Details of this constitutive model are given in the following subsection.

The first example regards a pull-out test on a concrete specimen. Experimentally, the crack evolves on a more or less bi-linear path. The results have been compared with both experimental and numerical data reported by [45,46].

The second application is on a single-edge notched specimen with not symmetric holes. The observed crack pattern consists of a crack deflecting towards the central hole overlapping the numerical one obtained by Dirik et al. [47].

The third application simulates a notched beam subjected to mixed-mode bending. In this case the results are compared with the experimental results reported by Li et al. [48] and with the numerical results obtained with the AA-FEM approach [28].

For each numerical application, the Young's modulus E, the Poisson's ratio ν, the elastic limit strain ε_0, the $\frac{\varepsilon_f}{\varepsilon_0}$ ratio, the interphase thickness w_b, the critical damage value D_{crit}, the elastic limit strain ε_0^{IPH} in the interphase and the radius R for the

Algorithm 3 Pseudo-Code at step n at the structure level

Read variables at convergence of step $n-1$
Set $\mathbf{K}_n^{(0)} \leftarrow \mathbf{K}_{n-1}$, $\mathbf{F}_n \leftarrow \mathbf{F}_{n-1}$, $\mathbf{Q}_n^{(0)} \leftarrow \mathbf{Q}_{n-1}$
▶ **ELASTIC PREDICTION**
$j \leftarrow 1$
Solve $\mathbf{K}_n^{(0)}\, \Delta\mathbf{U}_n^{(j)} = \Delta\mathbf{F}_n + \Delta\mathbf{Q}_n^{(j)}$
$\mathbf{U}_n^{(j)} \leftarrow \mathbf{U}_{n-1} + \Delta\mathbf{U}_n^{(j)}$
$\mathbf{F}_n \leftarrow \mathbf{F}_{n-1} + \Delta\mathbf{F}_n$
$\mathbf{Q}_n^{(j)} \leftarrow \mathbf{Q}_{n-1} + \Delta\mathbf{Q}_n^{(j)}$
if SUBS **then**
  $\left(\mathbf{K}_{SUB}, \mathbf{F}_{int}^{SUB}\right) \leftarrow$ CALL SOLVE-SUBS($\mathbf{U}_e^{SUB,j}$)
end if
Update damages at FEs and calculate $\left(\mathbf{K}_n^{(j)}, \mathbf{F}_{int}^{(j)}\right)$
Evaluate error $\mathbf{Err}^{(j)} = \mathbf{F}_n + \mathbf{Q}_n^{(j)} - \mathbf{F}_{int}^{(j)}$
if $\left|\mathbf{Err}_n^{(j)}\right| \geq tol$ **then** ▷ check convergence
  ▶ **NONLINEAR CORRECTION**
  $j \leftarrow j+1$
  Solve $\mathbf{K}_n^{(j-1)}\, \Delta\Delta\mathbf{U}_n^{(j)} = \mathbf{Err}^{(j-1)} + \Delta\Delta\mathbf{Q}_n^{(j)}$
  $\mathbf{U}_n^{(j)} \leftarrow \mathbf{U}_n^{(j-1)} + \Delta\Delta\mathbf{U}_n^{(j)}$
  $\mathbf{Q}_n^{(j)} \leftarrow \mathbf{Q}_n^{(j-1)} + \Delta\Delta\mathbf{Q}_n^{(j)}$
  if SUBS **then**
    $\left(\mathbf{K}_{SUB}, \mathbf{F}_{int}^{SUB}\right) \leftarrow$ CALL SOLVE-SUBS($\mathbf{U}_e^{SUB,j}$)
  end if
  Update damages at FEs and calculate $\left(\mathbf{K}_n^{(j)}, \mathbf{F}_{int}^{(j)}\right)$
  Evaluate error $\mathbf{Err}^{(j)} = \mathbf{F}_n + \mathbf{Q}_n^{(j)} - \mathbf{F}_{int}^{(j)}$
  go to 11
end if
▶ **CRACK – TRACKING**
$(r, \alpha) \leftarrow$ CALL CRACK-TRACKING ALGORITHM
if (new r).*or*.(new α) **then**
  go to 3
else
  Memorize data and exit
end if

nonlocal procedure are provided. Other variables such as D_{min} and D_{stab} are considered as a function of D_{crit} with the same relation valid for all the three applications:

$$D_{min} = 0.25 D_{crit}, \qquad D_{stab} = 0.5 D_{crit}. \tag{47}$$

Also, a maximum of 5 possible positions of the crack tip inside an element are considered.

5.1. Isotropic damage constitutive model

The implemented Isotropic Damage Model is the one formulated by Jirásek in [43] and Mazars in [44]. It is a strain-based damage model, therefore the damage variable $D \in [0, 1]$ is a function of the strain measured at the evaluation point.

In particular, the evolution of damage is calculated on the basis of an internal kinematic variable κ, which is equal to the maximum value ever reached by the *equivalent strain* $\tilde{\varepsilon}$ along the loading path. Using this definition, κ represents a memory variable over a period t:

$$\kappa = \max \tilde{\varepsilon}(t). \tag{48}$$

The equivalent strain is a scalar measure of the strain level and is here defined adopting the so-called *Mazars* definition:

$$\tilde{\varepsilon} = \sqrt{\sum_{I=1}^{3} \langle \varepsilon_I \rangle^2} \tag{49}$$

where ε_I (I = 1,2,3) are the principal strains at the specific evaluation point and the McAuley brackets $\langle \cdot \rangle$ denote the positive part. This definition allows us to consider the different behavior in tension and compression, typical for a quasi-brittle material.

Damage activation is regulated by the function:

$$f(\tilde{\varepsilon}, \kappa) = \tilde{\varepsilon} - \kappa, \tag{50}$$

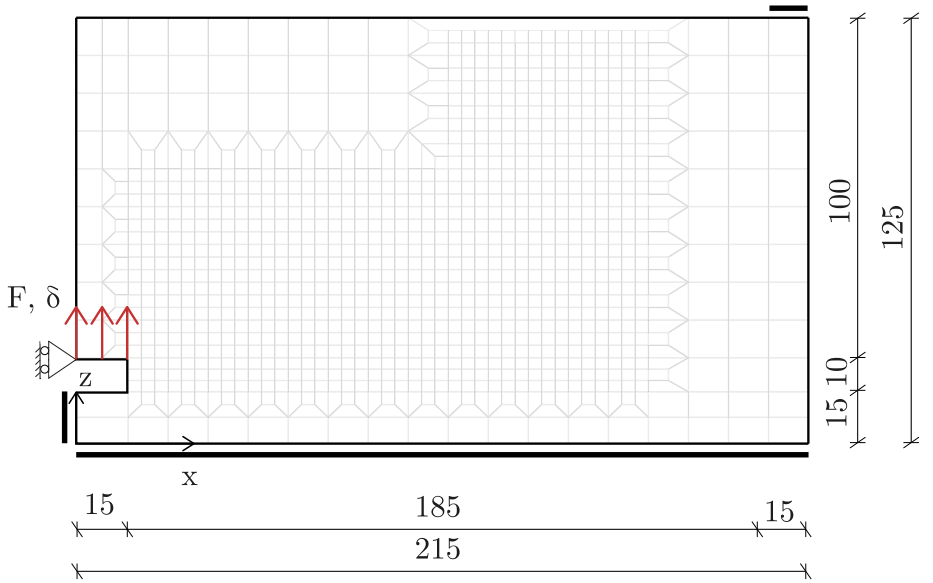

Fig. 9. Example 1 - Geometry and boundary conditions. Dimensions are in mm.

while the loading-unloading relations are given by the well-known Kuhn–Tucker conditions:

$$f(\tilde{\varepsilon},\kappa) \le 0, \quad \dot{\kappa} \ge 0, \quad \dot{\kappa}\, f(\tilde{\varepsilon},\kappa) = 0. \tag{51}$$

The function describing damage evolution can be explicitly written as

$$D = g(\kappa) = \begin{cases} 0 & \text{if } \kappa \le \varepsilon_0 \\ 1 - \frac{\varepsilon_0}{\kappa} \exp\left(-\frac{\kappa-\varepsilon_0}{\varepsilon_f-\varepsilon_0}\right) & \text{if } \kappa > \varepsilon_0, \end{cases} \tag{52}$$

being ε_0 and ε_f the elastic and post-elastic limit strains, respectively.

Consequently, the damaged secant stiffness tensor is expressed as

$$\mathbf{E}_s = (1 - D)\mathbf{E} \tag{53}$$

and the stress–strain relation can be written in the form

$$\boldsymbol{\sigma} = \mathbf{E}_s\, \boldsymbol{\varepsilon} = (1 - D)\, \mathbf{E}\, \boldsymbol{\varepsilon}. \tag{54}$$

The tangent stiffness matrix $\mathbf{E}_t$ is instead obtained as:

$$\boldsymbol{E}_t = \frac{\partial \boldsymbol{\sigma}}{\partial \boldsymbol{\varepsilon}} = (1 - D)\boldsymbol{E} - \boldsymbol{E}\boldsymbol{\varepsilon} \left(\frac{\partial D}{\partial \boldsymbol{\varepsilon}}\right)^T \tag{55}$$

where

$$\frac{\partial D}{\partial \boldsymbol{\varepsilon}} = \frac{\partial D}{\partial \kappa} \frac{\partial \kappa}{\partial \tilde{\varepsilon}} \frac{\partial \tilde{\varepsilon}}{\partial \boldsymbol{\varepsilon}}. \tag{56}$$

5.2. Pull-out test on a concrete specimen

This example simulates the pull-out test of an anchor bolt embedded in concrete, presented by RILEM Technical Committee 90-FMA [45]. The concrete specimen has a prismatic shape, with a thickness of 100 mm. Geometry, mesh, loading and displacement boundary conditions adopted in the numerical simulations are shown in Fig. 9. The specimen is unconstrained on the vertical edge above the anchor bolt, on the right vertical edge, and on the upper surface apart from the last two nodes. These, together with the bottom side and the vertical edge under the anchor bolt, are fully constrained. The load transferred by the anchor bolt to the concrete is reproduced by imposing incremental vertical displacement δ on the entire upper surface of the notch, until a final value of $\delta = 0.3$ mm.

Experimentally, a crack nucleates from the notch and initially proceeds in a roughly rectilinear way, with a slope $\alpha \simeq 13°$. After moving on for about 80 mm, the crack changes its direction, now pointing towards the upper right constraints. The result is a sort of bi-linear experimental path.

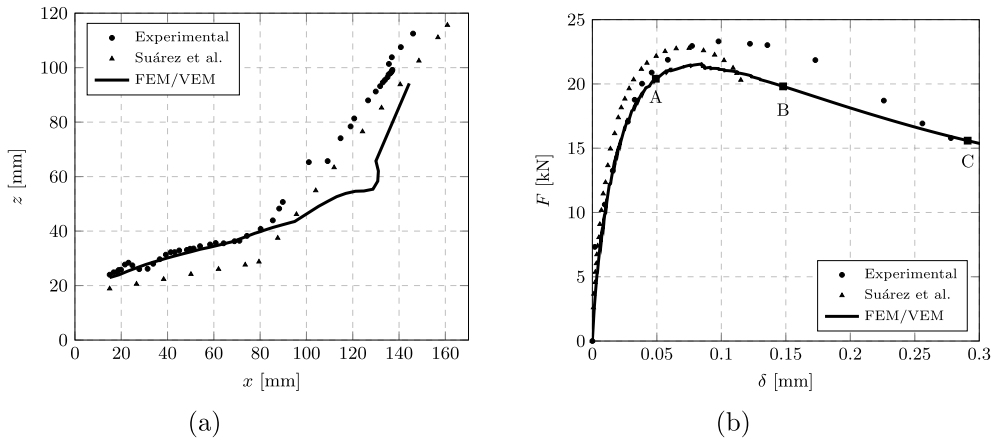

Fig. 10. Example 1 - Comparison between experimental [45] and numerical (a) crack patterns and (b) Load–displacement curves.

Table 1
Example 1 - Material parameters.

E [MPa]	ν	ϵ_0	$\frac{\epsilon_f}{\epsilon_0}$	w_b [mm]	D_{crit}	ϵ_0^{IPH}	R [mm]
30 000	0.2	$1.27E{-}4$	400	2.5	0.65	$0.89E{-}4$	10

Table 2
Example 2 - Material parameters.

E [MPa]	ν	ϵ_0	$\frac{\epsilon_f}{\epsilon_0}$	w_b [mm]	D_{crit}	ϵ_0^{IPH}	R [mm]
71 700	0.33	$7.20E{-}3$	100	0.4	0.5	$5.76E{-}3$	3

The parameters requested by the elasto-damaging constitutive model and also those governing damage nucleation and propagation are reported in Table 1. The main constitutive values are taken from [46]. The radius of the semicircle for the nonlocal evaluation of $\mathbf{n}_b$ has been chosen equal to around two times and a half the element size.

Numerical results are plotted in terms of crack pattern (Fig. 10a) and load–displacement curve (Fig. 10b). Numerical results obtained with the proposed coupled FEM-VEM approach are compared with the experimental data and the numerical results obtained with Suárez's cohesive crack model [46]. In [46], the crack path was pre-defined.

In this example the catching of the second branch is numerically difficult. Even Suárez's model, for example, is not able to catch this branch if that model is left free to localize, without a pre-defined path. In the proposed approach the crack initially evolves on the same experimental slope. The second part of the experimental pattern is not very well caught, but a change in the slope is anyway observed.

Load–displacement curves reported in Fig. 10b are also in good agreement with the experimental one.

Fig. 11 shows the deformed configurations at the markers A (a), B (b) and C (c) of Fig. 10b, together with the substructure configuration at the same time steps.

5.3. Single edge notched specimen with holes

In this example the proposed numerical approach is applied to simulate a single-edge notched specimen with asymmetric holes subjected to tensile loads (Fig. 12). This example was studied by Dirik et al. [47], who referred to the experimental investigations presented by Lu et al. [49]. It regards an aluminum alloy Al-7075-T6 square specimen 50×50 mm big, with a thickness of 5 mm and a notch 2 mm wide. Load was applied as two opposite forces obtained by pushing up or down the two holes having 10 mm as diameter, symmetrically placed with respect to the artificial notch. As a consequence, the crack experimentally evolves in a mixed-mode. Initially, it goes aligned to the notch. Then, it turns and finally strikes the smaller asymmetric hole with a diameter equal to 8 mm.

The constitutive parameters employed to run the numerical simulation are reported in Table 2, and coincide with those given by [47].

In order to reproduce the experimental path, the specimen is fully constrained in all the degrees of freedom of the upper half of the top hole and in the lower half of the bottom hole. On the same nodes an incremental vertical displacement δ is imposed, in opposite directions on the two holes, until the final value of $\delta = 1$ mm. Fig. 12 shows the geometry, mesh and boundary conditions

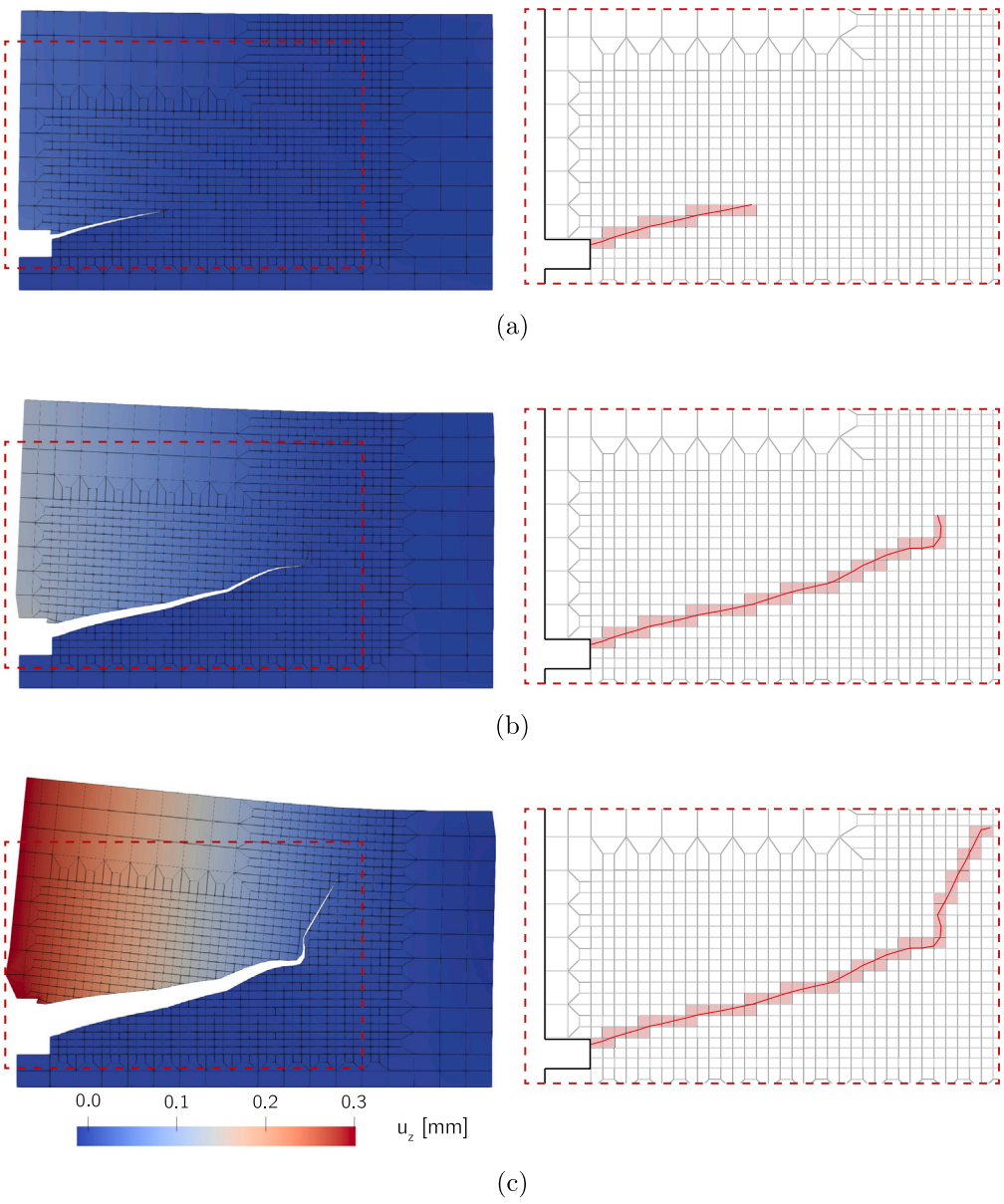

Fig. 11. Example 1 - Deformed shapes at points (a) A, (b) B, and (c) C indicated in Fig. 10b. Enlargements show the correspondent substructure configurations with evidenced VEs.

for this example. A finer mesh is chosen for the crack propagating zone, as visible in the zoom of the same Figure.

The experimental analyses carried out by [49] involved several specimens and aimed at evaluating the influence of the position of the holes on the crack pattern. The simulated test presented holes closer to the middle plane, resulting in a large impact on the mode II component. Fig. 13a shows a comparison between the experimental crack pattern, the numerical one obtained by Dirik et al. [47] and the numerical one obtained with the implemented FEM-VEM formulation. The crack path perfectly overlaps the numerical Dirik's crack pattern and almost all the experimental one, apart from the final part.

The corresponding load–displacement curve is reported in Fig. 13b, while Fig. 14 shows the deformed configurations at the markers A (*a*), B (*b*) and C (*c*) of Fig. 13b. No load–displacement curves are reported by [47], and no comparisons could be made.

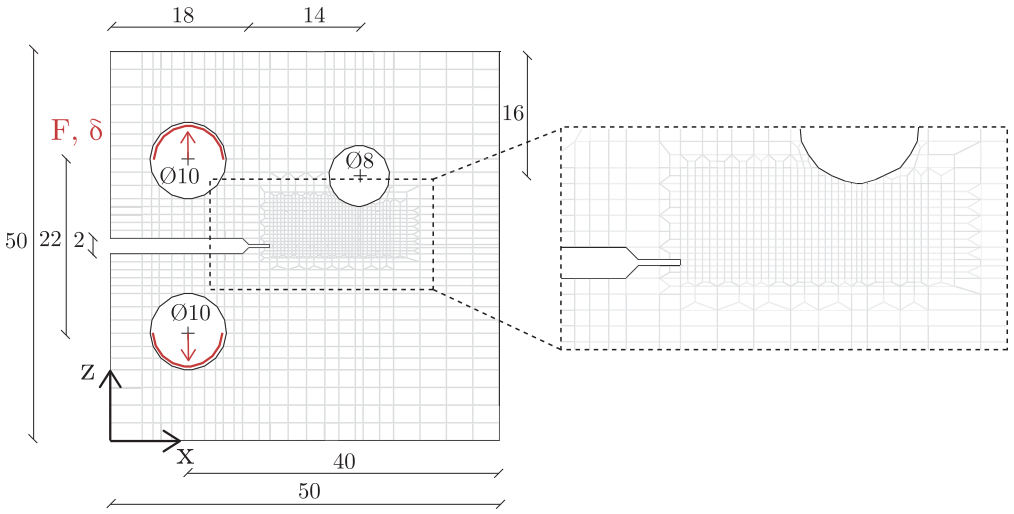

Fig. 12. Example 2 - Geometry and boundary conditions. Dimensions are in mm.

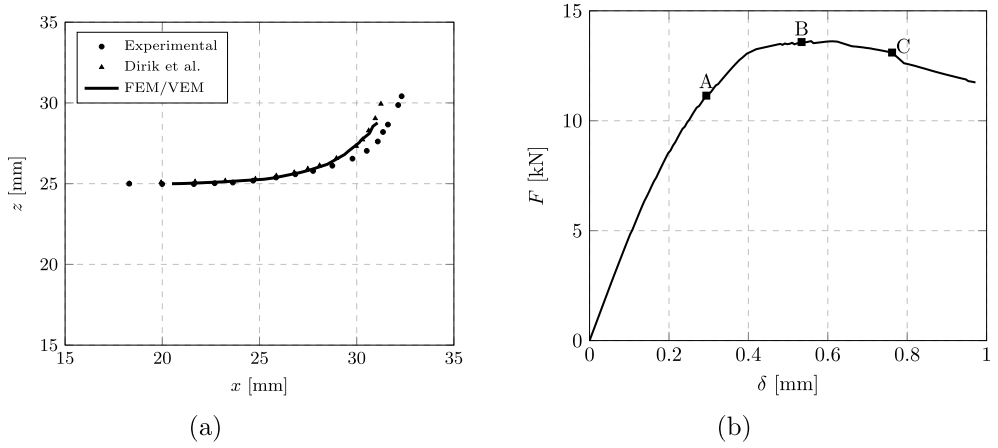

Fig. 13. Example 2 - (a) Comparison between experimental [49] and numerical crack patterns; (b) Load–displacement curve.

Table 3
Example 3 - Material parameters.

E [MPa]	ν	ϵ_0	$\frac{\epsilon_f}{\epsilon_0}$	w_b [mm]	D_{crit}	ϵ_0^{IPH}	R [mm]
38 000	0.2	$7.89E{-}5$	150	1	0.3	$7.89E{-}5$	20

5.4. Notched beam under mixed mode bending

This application regards a single edge notched beam subjected to mixed mode bending. This beam was experimentally tested by Gálvez et al. [50], whose results are reported by Li et al. [48]. The beam is 675 mm long and 150 mm high, with a thickness of 50 mm. It has a vertical notch of length equal to half of the beam height and width of 2 mm, positioned at the bottom center. The beam is fixed at a right support 37.5 mm far from the right edge, and vertically constrained at a left support 75 mm far from the center. The test was conducted under displacement control. An incremental vertical displacement δ is imposed on the top of the beam by pushing a steel frame here represented by four rigid elements, at a distance of 150 mm from the center of the beam, on the right side. Fig. 15 shows the geometry, mesh and boundary conditions.

The results of two experimental tests are commented on in [48], here reported in Fig. 16. These results are numerically simulated using the constitutive parameters listed in Table 3 and given by [48].

The crack pattern consists of a fracture that emerges from the notch tip and propagates at a skew angle towards the applied load area. Fig. 16a compares the numerical crack pattern with the experimental ones. The numerical trend is initially closer to one of the two experimental outcomes, while it overlaps the other experimental test at the end. In the middle, it remains between the two

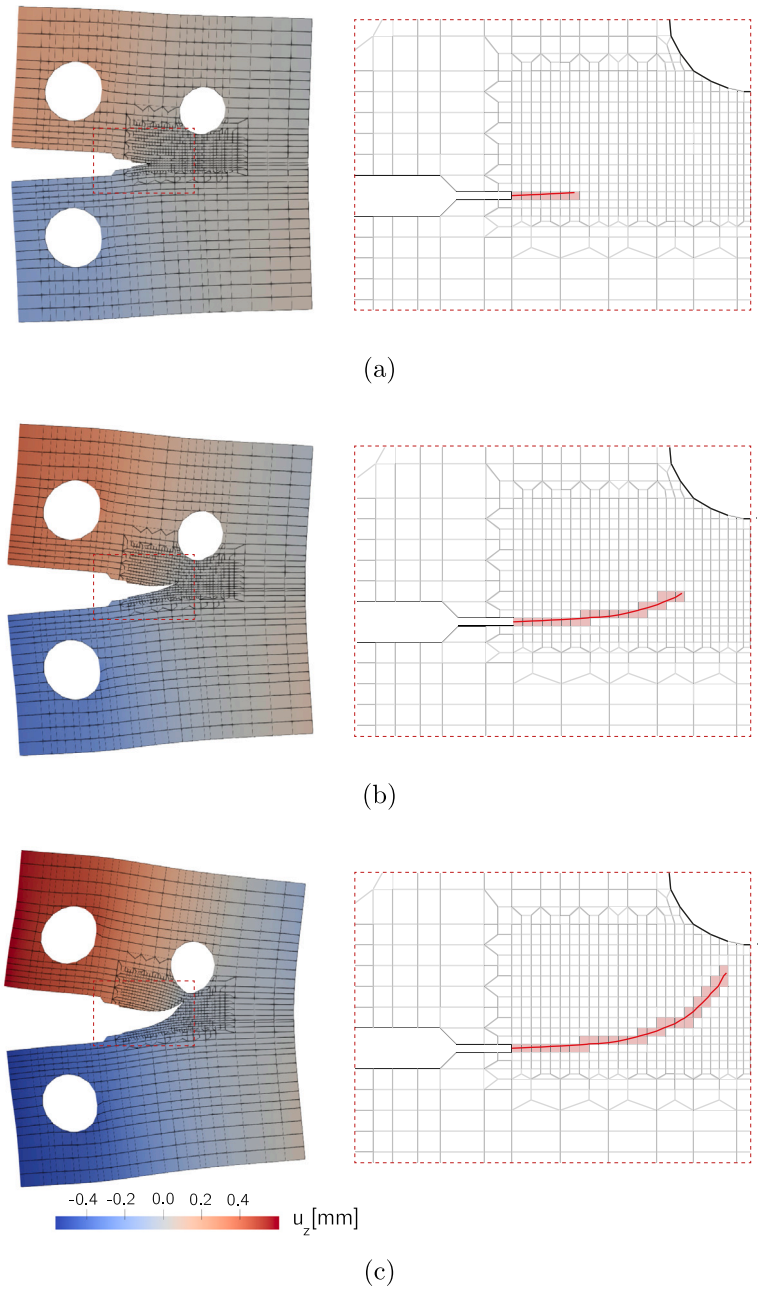

Fig. 14. Example 2 - Deformed shapes at points (a) A, (b) B, and (c) C indicated in Fig. 13b. Enlargements show the correspondent substructure configurations with evidenced VEs.

experimental curves.

During the test, the crack mouth opening displacement (CMOD) is measured. The corresponding load–CMOD curves are depicted in Fig. 16b. The numerical results overlap with the experimental ones in the elastic branch. Besides, the same initial nonlinear response and maximum load of one of the two experimental curves is caught. A good agreement is however obtained in the post-peak regime.

In the same figure, the results of a numerical analysis conducted using the AA-FEM approach [28] are reported. FEM/VEM and AA-FEM crack paths appear similar in the first part. AA-FEM undergoes a significant change in the second part, while FEM/VEM crack paths remain more close to the experimental trend. Similar load–CMOD curves are obtained, with a slight difference in peak load.

Fig. 17 shows the deformed configurations at the final stage of the curve reported in Fig. 16b.

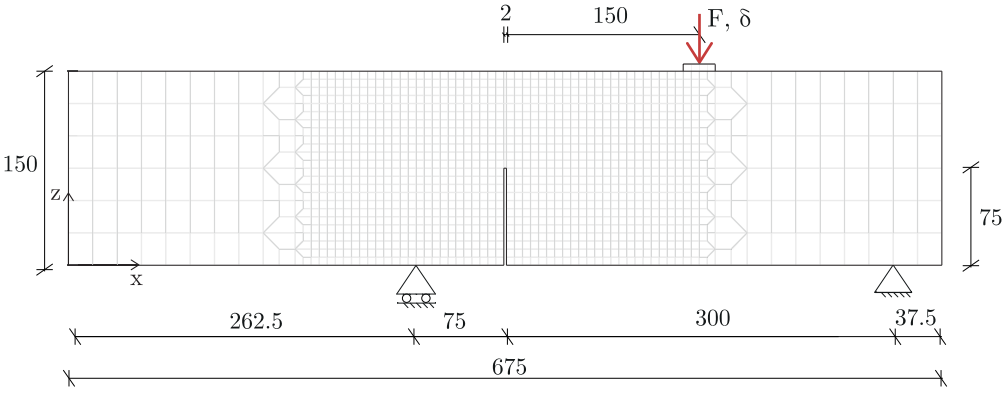

Fig. 15. Example 3 - Geometry and boundary conditions. Dimensions are in mm.

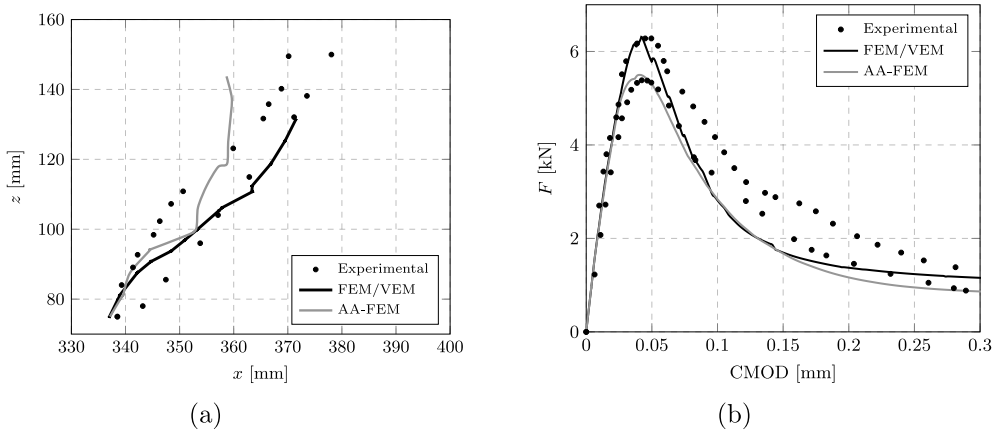

Fig. 16. Example 3 - Comparison between experimental [50] and numerical (a) crack patterns and (b) Load–CMOD curves.

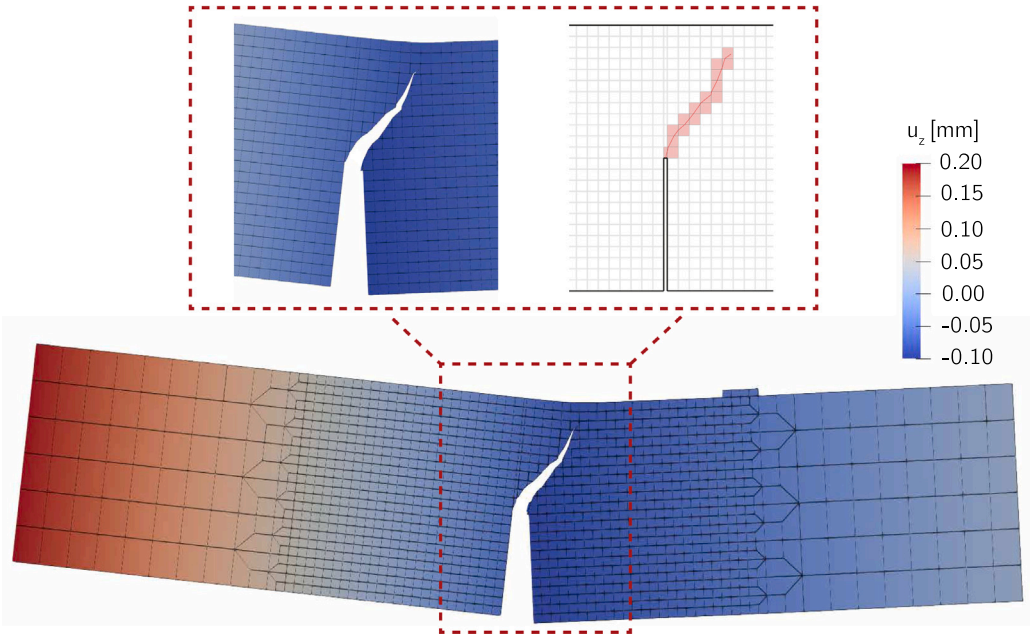

Fig. 17. Example 3 - Deformed shapes at the final stage of the curve in Fig. 16b. Enlargements show a detailed view of the crack and the correspondent substructure configuration with evidenced VEs.

6. Conclusions

In this work, an innovative approach to describe crack evolution in quasi-brittle materials, modeled in the framework of isotropic damage mechanics, has been presented.

Based on innovative FEM-VEM coupled discretization of the body, this technique gives satisfactory results. They are comparable to the results obtained by well established approaches in the literature, where crack propagation is correctly caught by usually employing remeshing procedures or adding degrees of freedom. These approaches usually require fine meshes to obtain accurate results, with an associated heavy computational effort.

By exploiting the possibility in the VEM to introduce polygonal elements without limitations on their shape, here minimal remeshing is needed, and cases where the crack tip is within the fracturing element can be easily modeled. The absence of a broad remeshing phase leads to computational time savings. The possibility of having a crack tip within the element guarantees the conformity of the mesh without particular mesh handling. The last benefit constitutes the main advancement with respect to the Augmented Advanced FEM approach recently proposed by the authors.

Moreover, with respect to the standard VEM, an enhanced VEM formulation has been implemented in this work, with the advantage of avoiding stiffness matrix stabilization and obtaining more accurate results thanks to the use of divergence-free and higher order polynomials.

Other advantageous points of the approach are the flexibility in implementing any constitutive model according to the specific problem studied, and the introduction of an interphase element instead of a more common zero-thickness interface. While a zero-thickness interface is able to model contact strains only, the interphase element adds internal strains that make the element more similar to a solid with simplified kinematics. In this view, the advantage is the possibility to use even the same constitutive model of the bulk material, with a reduced number of constitutive parameters that are certainly not easy to calibrate.

The specific strategy is built on the concepts of substructure and critical damage, and incorporates the benefits of delayed crack models. The implemented algorithm decides the propagation and orientation of the crack on the basis of a mix of a local and a nonlocal criterion, respectively.

The proposed numerical strategy has been applied to three applications for which experimental and numerical results were available in the literature. By comparing the numerical responses with the available experimental and numerical data, in terms of load–displacement curves and fracture patterns, a good agreement has been observed. In all numerical tests, the code was confirmed to be fast, with quadratic convergence at both the structure and substructure levels.

The proposed approach could be further enriched to permit the evolution of multiple cracks or crack branching. Certainly, additional investigations are necessary to establish the eventual dependence of the approach on some model parameters (i.e. the values of D_{min} and D_{stab}) and on the mesh size. Finally, other applications could be conducted in the framework of elastoplasticity or coupled with elastoplasticity and damage mechanics.

CRediT authorship contribution statement

Antonino Spada: Writing – review & editing, Writing – original draft, Validation, Supervision, Software, Methodology, Funding acquisition, Formal analysis, Data curation, Conceptualization. **Marianna Puccia:** Writing – review & editing, Writing – original draft, Validation, Data curation. **Elio Sacco:** Writing – review & editing, Validation, Supervision, Methodology, Funding acquisition, Formal analysis, Conceptualization. **Giuseppe Giambanco:** Writing – review & editing, Validation, Supervision, Methodology, Funding acquisition, Formal analysis, Conceptualization.

Funding

The authors acknowledge the financial support given by the Italian Ministry of University and Research (MUR) under the PRIN22 project 2022P7PF8J_002, LAttice STructures for Energy aBsorption: advanced numerical analysis and optimal design (LASTEB).

Declaration of competing interest

The authors declare that they have no known competing financial interests or personal relationships that could have appeared to influence the work reported in this paper.

Appendix

A key point of the enhanced VEM procedure is the evaluation of the stiffness matrix in Eq. (20). In [33], when the polynomial boundary shape functions are of degree $k = 1$, the suggested order of the divergence-free polynomials is $p = 1$ for elements having at maximum 5 edges/nodes, $p = 2$ for elements with 6 or 7 edges/nodes.

In this work, starting from a quadrilateral element, VEs can have 3, 4, 5, or 7 nodes. Consequently, $p = 2$ is used for the element with 7 nodes, $p = 1$ for the others. As such, the adopted matrices of the polynomial approximation $\check{\mathbf{N}}$ are:

- if $p = 1$:

$$\check{\mathbf{N}} = \begin{bmatrix} 1 & 0 & 0 & z & 0 & x & 0 \\ 0 & 1 & 0 & 0 & x & 0 & z \\ 0 & 0 & 1 & 0 & 0 & -z & -x \end{bmatrix} \tag{A.1}$$

- if $p = 2$:

$$\check{\mathbf{N}} = \begin{bmatrix} 1 & 0 & 0 & z & 0 & x & 0 & 2xz & 0 & x^2 & z^2 & 0 \\ 0 & 1 & 0 & 0 & x & 0 & z & 0 & 2xz & z^2 & 0 & x^2 \\ 0 & 0 & 1 & 0 & 0 & -z & -x & -z^2 & -x^2 & -2xz & 0 & 0 \end{bmatrix} \tag{A.2}$$

To obtain the stiffness matrix of Eq. (20) it is necessary to evaluate three integrals, two on the element area (among which matrix **G**), and one on its boundary (matrix **B**).

Considering the polynomial order of the shape functions, to evaluate matrix **B** the functions to be integrated will be at maximum of order 3, and two Gauss points are sufficient for each edge to obtain the exact integral, even with an element with 7 nodes.

To evaluate **G** and the integral inside $\mathbf{K}_{VE}$, the functions to be integrated can be of order 2 or of order 4. Since the VE can also have a not standard shape, a Delaunay triangulation [51] of the element area is firstly operated. Then, in order to obtain the exact integral, when functions are of order 2 three Gauss points are employed on the correspondent isoparametric triangular element, while when functions are of order 4 seven Gauss points are used.

The following average computing times are needed to evaluate the stiffness matrix and force vector in a virtual element on the basis of the number of its nodes: 0.0320 s (3 nodes), 0.0385 s (4 nodes), 0.0390 s (5 nodes), 0.0449 s (7 nodes).

It is important to note that the element having 7 nodes is unique in the entire mesh, and is evaluated once at every iteration. When a finite element is split into two quadrilateral elements the average total time is 0.077 s When a finite element is split into a triangular and a pentagonal element the average total time is 0.071 s It takes about the same average time to run a totally cracked element, but it takes even less time to run an element with seven nodes which is also once evaluated.

Data availability

Data will be made available on request.

References

[1] A. Lyapunov, On the General Problem of Stability of Motion (Master's thesis), Kharkov Mathematical Society, Soviet Union, 1892.
[2] J. Hadamard, Leçons sur la Propagation des Ondes et les Équations de l'Hydrodynamique, A. Hermann, 1903.
[3] R. Hill, A general theory of uniqueness and stability in elastic-plastic solids, J. Mech. Phys. Solids 6 (3) (1958) 236–249.
[4] T.Y. Thomas, Plastic Flow and Fracture in Solids, Elsevier, 1961.
[5] J.W. Rudnicki, J. Rice, Conditions for the localization of deformation in pressure-sensitive dilatant materials, J. Mech. Phys. Solids 23 (6) (1975) 371–394.
[6] G. Borré, G. Maier, On linear versus nonlinear flow rules in strain localization analysis, Meccanica 24 (1) (1989) 36–41.
[7] E. Rizzi, I. Carol, K. Willam, Localization analysis of elastic degradation with application to scalar damage, J. Eng. Mech. 121 (4) (1995) 541–554.
[8] R. De Borst, Bifurcations in finite element models with a non-associated flow law, Int. J. Numer. Anal. Methods Geomech. 12 (1) (1988) 99–116.
[9] Z.P. Bazănt, G. Pijaudier-Cabot, Nonlocal continuum damage, localization instability and convergence, J. Appl. Mech. (1988).
[10] E.C. Aifantis, Update on a class of gradient theories, Mech. Mater. 35 (3–6) (2003) 259–280.
[11] R.d. Borst, J.J. Remmers, A. Needleman, M.-A. Abellan, Discrete vs smeared crack models for concrete fracture: bridging the gap, Int. J. Numer. Anal. Methods Geomech. 28 (7–8) (2004) 583–607.
[12] P.A. Cundall, R.D. Hart, Numerical modeling of discontinua, in: Analysis and Design Methods, Elsevier, 1993, pp. 231–243.
[13] T. Rabczuk, T. Belytschko, Cracking particles: a simplified meshfree method for arbitrary evolving cracks, Int. J. Numer. Methods Eng. 61 (13) (2004) 2316–2343.
[14] Y. Zhang, X. Zhuang, Cracking elements: A self-propagating strong discontinuity embedded approach for quasi-brittle fracture, Finite Elem. Anal. Des. 144 (2018) 84–100.
[15] G.I. Barenblatt, The formation of equilibrium cracks during brittle fracture. General ideas and hypotheses. Axially-symmetric cracks, J. Appl. Math. Mech. 23 (3) (1959) 622–636.
[16] D.S. Dugdale, Yielding of steel sheets containing slits, J. Mech. Phys. Solids 8 (2) (1960) 100–104.
[17] A. Hillerborg, M. Modéer, P.-E. Petersson, Analysis of crack formation and crack growth in concrete by means of fracture mechanics and finite elements, Cem. Concr. Res. 6 (6) (1976) 773–781.
[18] F. Lebon, M. Raffa, R. Rizzoni, A family of models of hard and soft interfaces with damage, Theor. Appl. Fract. Mech. 127 (2023) 104008.
[19] N. Moës, T. Belytschko, Extended finite element method for cohesive crack growth, Eng. Fract. Mech. 69 (7) (2002) 813–833.
[20] E. Benvenuti, N. Orlando, A mesh-independent framework for crack tracking in elastodamaging materials through the regularized extended finite element method, Comput. Mech. 68 (2021) 25–49.
[21] T. Strouboulis, K. Copps, I. Babuška, The generalized finite element method, Comput. Methods Appl. Mech. Engrg. 190 (32–33) (2001) 4081–4193.
[22] T.-P. Fries, T. Belytschko, The extended/generalized finite element method: an overview of the method and its applications, Internat. J. Numer. Methods Engrg. 84 (3) (2010) 253–304.
[23] J.M. Melenk, I. Babuška, The partition of unity finite element method: basic theory and applications, Comput. Methods Appl. Mech. Engrg. 139 (1–4) (1996) 289–314.
[24] D. Ling, Q. Yang, B. Cox, An augmented finite element method for modeling arbitrary discontinuities in composite materials, Int. J. Fract. 156 (2009) 53–73.
[25] W. Liu, Q. Yang, S. Mohammadizadeh, X. Su, An efficient augmented finite element method for arbitrary cracking and crack interactions in solids, Internat. J. Numer. Methods Engrg. 80 (4) (2013).
[26] S. Essongue, G. Couégnat, E. Martin, Performance assessment of the augmented finite element method for the modeling of weak discontinuities, Internat. J. Numer. Methods Engrg. 122 (2021) 172–189.
[27] Z. Ma, Q. Yang, X. Su, A conforming augmented finite element method for modeling arbitrary cracking in solids, J. Appl. Mech. 86 (2019) 071002.
[28] M. Puccia, A. Spada, G. Giambanco, Finite elements with embedded interphases for strain localization in quasi-brittle materials, Eng. Fract. Mech. (2022) 108956.
[29] G. Giambanco, Z. Mróz, The interphase model for the analysis of joints in rock masses and Masonry structures, Meccanica 36 (2001) 111–130.

[30] G. Giambanco, G.F. Scimemi, A. Spada, The interphase finite element, Comput. Mech. 50 (3) (2012) 353–366.
[31] L. Beirão da Veiga, F. Brezzi, A. Cangiani, G. Manzini, L.D. Marini, A. Russo, Basic principles of virtual element methods, Math. Models Methods Appl. Sci. 23 (01) (2013) 199–214.
[32] E. Artioli, S. Marfia, E. Sacco, VEM-based tracking algorithm for cohesive/frictional 2D fracture, Comput. Methods Appl. Mech. Engrg. 365 (2020) 112956.
[33] A. D'Altri, S. de Miranda, L. Patruno, E. Sacco, An enhanced VEM formulation for plane elasticity, Comput. Methods Appl. Mech. Engrg. 376 (2021) 113663.
[34] M. Cremonesi, A. Lamperti, C. Lovadina, U. Perego, A. Russo, Analysis of a stabilization-free quadrilateral virtual element for 2D linear elasticity in the Hu–Washizu formulation, Comput. Math. Appl. 155 (2024) 142–149.
[35] A. Lamperti, M. Cremonesi, U. Perego, A. Russo, C. Lovadina, A Hu–Washizu variational approach to self-stabilized virtual elements: 2D linear elastostatics, Comput. Mech. 71 (2023) 935–955.
[36] S. Marfia, E. Monaldo, E. Sacco, Cohesive fracture evolution within virtual element method, Eng. Fract. Mech. (2022) 108464.
[37] F. Liguori, A. Madeo, S. Marfia, E. Sacco, A hybrid virtual element formulation for 2D elasticity problems, Comput. Methods Appl. Mech. Engrg. 426 (2024) 116970.
[38] S. Saloustros, L. Pelà, M. Cervera, P. Roca, Finite element modelling of internal and multiple localized cracks, Comput. Mech. 59 (2) (2017) 299–316.
[39] E. Tamayo-Mas, J. Feliu-Fabá, M. Casado-Antolin, A. Rodríguez-Ferran, A continuous-discontinuous model for crack branching, Internat. J. Numer. Methods Engrg. 120 (1) (2019) 86–104.
[40] Y. Wang, H. Waisman, From diffuse damage to sharp cohesive cracks: a coupled XFEM framework for failure analysis of quasi-brittle materials, Comput. Methods Appl. Mech. Engrg. 299 (2016) 57–89.
[41] M. Jirásek, T. Zimmermann, Rotating crack model with transition to scalar damage, J. Eng. Mech. 124 (3) (1998) 277–284.
[42] F. Freddi, E. Sacco, An interface damage model accounting for in-plane effects, Int. J. Solids Struct. 51 (25-26) (2014) 4230–4244.
[43] M. Jirásek, Damage and smeared crack models, in: Numerical Modeling of Concrete Cracking, Springer, 2011, pp. 1–49.
[44] J. Mazars, A description of micro-and macroscale damage of concrete structures, Eng. Fract. Mech. 25 (5–6) (1986) 729–737.
[45] L. Elfgren, R. Eligehausen, J.G. Rots, Anchor bolts in concrete structures: summary of round robin tests and analysis arranged by RILEM TC 90-FMA 'fracture mechanics of concrete-applications', Mater. Struct. 34 (8) (2001) 451–457.
[46] F. Suárez, J. Gálvez, D. Cendón, A material model to reproduce mixed-mode fracture in concrete, Fatigue Fract. Eng. Mater. Struct. 42 (1) (2019) 223–238.
[47] H. Dirik, T. Yalçinkaya, Crack path and life prediction under mixed mode cyclic variable amplitude loading through XFEM, Int. J. Fatigue 114 (2018) 34–50.
[48] W.-S. Li, J.-Y. Wu, A consistent and efficient localized damage model for concrete, Int. J. Damage Mech. 27 (4) (2018) 541–567.
[49] Z. Lu, J. Xu, L. Wang, J. Zhang, Y. Liu, Curvilinear fatigue crack growth simulation and validation under constant amplitude and overload loadings, J. Aerosp. Eng. 28 (1) (2015) 04014054.
[50] J. Gálvez, M. Elices, G. Guinea, J. Planas, Mixed mode fracture of concrete under proportional and non proportional loading, Int. J. Fract. 94 (1998) 267–284.
[51] D. Lee, B. Schachter, Two algorithms for constructing a delaunay triangulation, Int. J. Comput. Inf. Sci. 9 (3) (1980) 219–242.